

**ŁODZ UNIVERSITY OF TECHNOLOGY**

**FACULTY OF ELECTRICAL, ELECTRONIC,  
COMPUTER AND CONTROL ENGINEERING**

**MASTER OF ENGINEERING THESIS**

**Numerical Assessment of Kidney Function  
from DCE-MRI**

**Katarzyna Sprawka**

**Student's number: 213407**

**Supervisor:**

**Prof. dr hab. inż. Andrzej Materka**

**Auxiliary supervisor:**

**Dr inż. Marek Kociński**

**Łódź, 2018**



ŁODZ UNIVERSITY OF TECHNOLOGY  
FACULTY OF ELECTRICAL, ELECTRONIC, COMPUTER AND CONTROL ENGINEERING

## Katarzyna Sprawka

MASTER OF ENGINEERING THESIS

### Numerical Assessment of Kidney Function from DCE-MRI

Łódź, 2018 r.

Prof. dr hab. inż. Andrzej Materka  
Dr inż. Marek Kociński

#### Abstract

The kidneys maintain whole body homeostasis enabling the organism to function in an optimal environment. The metrics of the renal function is glomerular filtration rate (GFR) and its monitoring is essential for prognosis, diagnosis and treatment of renal diseases. Clinically used chemical methods are cumbersome and do not allow for single kidney GFR (SKGFR) estimation, in contrary to the analysis of the dynamic contrast enhanced magnetic resonance imaging (DCE-MRI), which enables a non-invasive examination of both renal function and structure in a single imaging session. However, there is a lack of methods enabling reliable renal function quantification without human interference.

The works included in this thesis are a part of the project, which aims to develop entirely data-driven method of GFR estimation directly from DCE-MRI—fast, efficient and accurate enough to be used in clinical practice. The scope of this thesis was to develop a library for quantitative analysis of DCE-MRI in the Python programming language to be used in the target method and to compare the performance of different pharmacokinetic (PK) models in renal function assessment applications.

First, the labels of both kidneys and aorta were depicted on the registered DCE-MRI sequences. In order to remove the region of the renal pelvis, the kidney voxel-wise segmentation on the basis of intensity time courses was performed with the use of principal component analysis (PCA) and k-means clustering algorithm. Average contrast agent concentration-time curves of the functional region of each kidney were then fitted to the four PK models: *Tofts and Kermode* (TK), *extended Tofts and Kermode* (ETK), *Patlak-Rutland* (PR) and *two-compartment exchange* (2CXM) models. From the obtained model parameters, the SKGFR and total GFR were calculated.

The developed method was tested on the DCE-MRI sequences of ten healthy subjects. Obtained total GFR values were compared with the values obtained in iohexol-GFR and serum-creatinine tests. The results showed that 2CXM is the most accurate and precise of tested PK models with reference to the iohexol-GFR and its performance is comparable with a serum-creatinine test.

The conclusion was drawn that 2CXM can be used in a final step of the GFR estimation in the target method and the developed library enables its implementation.

**Keywords:** DCE-MRI, kidney, glomerular filtration rate, pharmacokinetic modelling, quantitative analysis, kidney segmentation.



## Katarzyna Sprawka

PRACA DYPLOMOWA MAGISTERSKA

### Numeryczna ocena funkcjonowania nerek na podstawie obrazów DCE-MRI

Łódź, 2018

Opiekun: Prof. dr hab. inż. Andrzej Materka  
Opiekun dodatkowy: Dr inż. Marek Kociński

#### Streszczenie

Nerki są odpowiedzialne za utrzymanie homeostazy całego ciała umożliwiając organizmowi funkcjonowanie w optymalnych warunkach. Miarą wydolności nerek jest współczynnik przesączania kłębuzkowego (GFR), a jego monitorowanie jest niezbędne w przewidywaniu, diagnostyce oraz leczeniu chorób nerek. Obecnie klinicznie używane metody chemiczne są kłopotliwe, a ponadto nie umożliwiają pomiaru GFR dla każdej nerki z osobna, w przeciwieństwie do analizy obrazów rezonansu magnetycznego o kontraste dynamicznie wzmacnionym środkiem cieniącym (DCE-MRI), która umożliwia nieinwazyjną ocenę struktury oraz funkcjonowania nerek w jednej sesji obrazowej. Jednakże brakuje metod, które umożliwiłyby oszacowanie GFR z obrazów DCE-MRI bez ingerencji operatora na pewnym z etapów przetwarzania obrazów.

Działania przedstawione w przedłożonej pracy są częścią projektu mającego na celu opracowanie komputerowej metody pomiaru GFR bezpośrednio z obrazów DCE-MRI, będącej na tyle dokładną, szybką i efektywną, aby znaleźć zastosowanie kliniczne. Celem pracy było stworzenie biblioteki w języku Python, umożliwiającej komputerową analizę ilościową obrazów DCE-MRI oraz porównanie różnych modeli farmakokinetycznych (PK) w zastosowaniu do oceny wydolności nerek.

W pierwszej kolejności zaznaczono obszary obu nerek oraz aorty na obrazie DCE-MRI po korekcji ruchu, a następnie w celu usunięcia obszaru miedniczki nerkowej przeprowadzono segmentację na podstawie przebiegów czasowych intensywności sygnału poszczególnych wokseli posługując się analizą głównych składowych oraz algorytmem k-średnich. Średnie przebiegi czasowe stężenia środka cieniącego w obszarze funkcjonalnym każdej z nerek dopasowano do 4 modeli PK: *Tofts and Kermode* (TK), *extended Tofts and Kermode* (ETK), *Patlak-Rutland* (PR) and *two-compartment exchange model* (2CXM). Na podstawie otrzymanych parametrów wyliczono GFR dla każdej z nerek oraz całkowity GFR.

Opracowaną metodę przetestowano na sekwencjach DCE-MRI dziesięciu zdrowych osób, a otrzymane wartości całkowitego GFR porównano z wartościami otrzymanymi metodami analizy klirensu iohexolu oraz stężenia kreatyniny. Otrzymane wyniki pokazały, że 2CXM jest najbardziej precyzyjnym z modeli, w odniesieniu do analizy klirensu iohexolu, a rezultaty otrzymane z jego zastosowaniem są zbliżone do analizy stężenia kreatyniny.

Podsumowując stwierdzono, że 2CXM może być użyty w ostatnim kroku docelowej metody estymującej GFR z obrazów DCE-MRI, a stworzona biblioteka umożliwia jego zaimplementowanie.

**Słowa kluczowe:** DCE-MRI, nerka, współczynnik przesączania kłębuzkowego, GFR, modelowanie farmakokinetyczne, analiza ilościowa, segmentacja nerek.



# Acknowledgements

First and foremost, I would like to express my sincere gratitude to Professor of the University of Bergen, Arvid Lundervold, for his enlightening guidance throughout this project and warm hosting me during the stay in Norway, for his encouragement and enthusiastic approach, immense knowledge, and most importantly for inspiring me with the world of medical imaging.

I also would like to thank my supervisors from my mother university, Professor Andrzej Materka and PhD. Marek Kociński for the useful comments and remarks both the substantive and editorial ones, which helped to give this dissertation its final shape. Without their assistance this thesis would have never been accomplished.



# Contents

<b>Abstract</b>	<b>i</b>
<b>Streszczenie</b>	<b>iii</b>
<b>Acknowledgement</b>	<b>v</b>
<b>Contents</b>	<b>vii</b>
<b>Abbreviations</b>	<b>x</b>
<b>1 Introduction</b>	<b>1</b>
1.1 Aims and scope of the thesis . . . . .	3
<b>2 The blood filter</b>	<b>4</b>
2.1 Structure of the kidney . . . . .	4
2.1.1 The nephron . . . . .	6
2.2 Functions of the kidney . . . . .	7
2.2.1 Urine formation . . . . .	10
2.2.2 Glomerular filtration rate . . . . .	12
<b>3 Dynamic contrast enhanced MRI</b>	<b>14</b>

3.1	Fundamentals of MRI . . . . .	14
3.1.1	$T_1$ - and $T_2$ -weighted images . . . . .	17
3.2	Fundamentals of dynamic contrast enhanced MRI . . . . .	20
3.2.1	DCE-MRI analysis . . . . .	21
3.2.1.1	Qualitative analysis . . . . .	21
3.2.1.2	Semi-quantitative analysis . . . . .	22
3.2.1.3	Quantitative analysis . . . . .	23
3.2.2	DCE-MRI applications . . . . .	23
<b>4</b>	<b>Pharmacokinetic modelling</b>	<b>25</b>
4.1	The tracer kinetic theory . . . . .	27
4.1.1	Linear stationary systems . . . . .	29
4.1.2	One-compartment model . . . . .	30
4.2	Arterial Input Function . . . . .	31
4.3	Intensity to concentration conversion . . . . .	32
<b>5</b>	<b>Materials and methods</b>	<b>34</b>
5.1	DCE-MRI renography . . . . .	34
5.2	DCE-MRI acquisition . . . . .	35
5.3	GFR reference values . . . . .	37
5.4	Image processing and analysis . . . . .	37
5.4.1	Motion correction . . . . .	37
5.4.2	Manual labelling . . . . .	38
5.4.3	Pelvis region removal . . . . .	39
5.4.4	Concentration-time curves . . . . .	44

5.4.5	Pharmacokinetic modelling . . . . .	47
5.4.6	GFR estimation . . . . .	53
<b>6</b>	<b>Results</b>	<b>54</b>
<b>7</b>	<b>Discussion</b>	<b>60</b>
7.1	Future work . . . . .	62
<b>8</b>	<b>Summary</b>	<b>63</b>
<b>References</b>		<b>65</b>
<b>Appendices</b>		<b>71</b>
<b>List of Figures</b>		<b>74</b>
<b>List of Tables</b>		<b>75</b>

# Abbreviations

<b>2CXM</b>	Two-compartment exchange (model)
<b>AIF</b>	Arterial input function
<b>AUC</b>	Area under the curve
<b>BSA</b>	Body surface area
<b>CA</b>	Contrast agent
<b>CC</b>	Cross-correlation
<b>CNN</b>	Convolutional neural network
<b>DCE-MRI</b>	Dynamic contrast enhanced magnetic resonance imaging
<b>DCT</b>	Distal convoluted tubule
<b>EES</b>	Extravascular extra-cellular space
<b>eGFR</b>	Estimated glomerular filtration rate
<b>ETK (model)</b>	Extended Toft-Kermode (model)
<b>FID</b>	Free induction decay
<b>Gd</b>	Gadolinium
<b>Gd-DOTA</b>	Gadoteric acid
<b>GFR</b>	Glomerular filtration rate
<b>Hct</b>	Hematocrit
<b>IAUC</b>	Initial area under the uptake curve

<b>IRF</b>	Impulse response function
<b>LoA</b>	Limits of agreement
<b>mGFR</b>	Measured glomerular filtration rate
<b>MRI</b>	Magnetic resonance imaging
<b>PC</b>	Principal component
<b>PCA</b>	Principal component analysis
<b>PCT</b>	Proximal convoluted tubule
<b>PK (models/modelling)</b>	Pharmacokinetic (models/modelling)
<b>PR (model)</b>	Patlak-Rutland (model)
<b>RF</b>	Radio-frequency
<b>ROI</b>	Region of interest
<b>SCr</b>	Serum-creatinine
<b>SD</b>	Standard deviation
<b>SKGFR</b>	Single kidney glomerular filtration rate
<b>SyN</b>	Symmetric normalisation
<b>TK (model)</b>	Toft-Kermode (model)



# Chapter 1

## Introduction

**A**CCORDING TO THE BELIEFS OF ANCIENT HEBREWS, the kidneys are the seat of the human soul and consciousness. They were also associated with the feeling of the fear and sadness [1]. Today, more mundane, but not less important tasks are being assigned to them.

Kidneys, although often underestimated, are the fundamental organs of human body and their working mechanism is extremely complex. Their essential task is to remove wastes from the organism but their functionality is much wider. They are also involved in maintaining acid-based balance, regulating the blood pressure and are major endocrine organs, which secret three important hormones: *erythropoietin*, *calcitriol* and *renin* [2]. In short terms, they maintain whole body homoeostasis, which is essential for overall health of the organism.

Gradually progressing loss of kidney function known as a chronic kidney disease is a growing world-wide problem. As much as 8–16 % of whole population suffers from this condition [3]. It significantly decreases comfort of life and in extreme cases leads to death. What is more, it was shown that renal diseases are risk factor for development of cardiovascular diseases [4]. Because of the fact that symptoms do not resemble renal failure, approximately 90% of the ill are unconscious of it until

the late stages [5]. That is why there is the demand for methods, which enable fast and accurate measurement of renal function required for all of three: prevention, monitoring and therapy.

The metrics of the level of kidney function is *glomerular filtration rate* (GFR) [6]. Good performance of the several important functions of the kidney are dependent on the GFR value. Not only does it allow for assessment of how well our kidneys are working, but also it can determine the stage of kidney disease. The gold standard of GFR measurement incorporates injection of the exogenous marker that is freely filtered by the kidney, and that does not undergo metabolism, tubular secretion or absorption. An example of such a marker can be *inulin*. However, in clinical practice usually the endogenous marker such a creatinine or urea is used and GFR is estimated applying robust algorithms [7]. Although chemical methods allow for accurate GFR estimation, they are not very practical in clinical use. Not only are they time-consuming and expensive but also they can be cumbersome. What is more, they provide information about combined GFR value and cannot be used for a single kidney function assessment. Thus, other methods are desired [8].

An innovative approach in estimating renal function is performing dynamic contrast-enhanced magnetic resonance (DCE-MRI), which provides time-varying images of the abdominal. The analysis of the obtained time-intensity changes as a function of time provides important information about renal performance [8, 9]. Traditionally, this evaluation is performed by an experienced observer, although this method is very subjective and strongly depends on the experience of the expert. Other technique involves fitting tissue intensity changes to *pharmacokinetic* (PK) models, which allows for quantification of renal function [9]. Even though this strategy is gaining more and more supporters, most of the methods still require interference of the human at some stage, which makes them vulnerable to human factors.

## 1.1 Aims and scope of the thesis

The works included in this thesis are a part of the bigger project realised at the University of Bergen in Norway, which aims to develop entirely data-driven method of GFR estimation directly from DCE-MRI, which would be fast and efficient and accurate enough to be used in clinical applications.

The overarching aims of this thesis were to create the library for GFR estimation by pharmacokinetic modelling in the Python programming language and to compare the performance of different PK models in renal function estimation. What is more, it should be decided whether any of them is accurate enough to be used in the target method of a fast GFR estimation.

The structure of this thesis is as follows: because of the fact that the thesis is connected with the assessment of the renal function, Chapter 2 deals with the basics of the renal anatomy and physiology in order to understand the mechanism of glomerular filtration and importance of the metric, which is GFR. Chapter 3 focuses on the basic principles of operation of DCE-MRI and introduces the current trends and obstacles in its examination. Furthermore, Chapter 4 is devoted to the issue of quantitative analysis of DCE-MRI. It discusses the basics of tracer kinetic theory and lists all components required for pharmacokinetic modelling. Next, Chapter 5 and Chapter 6 focus on the practical part of the work. Chapter 5 describes in details the subsequent steps of DCE-MRI processing, whereas Chapter 6 presents obtained results. Finally, in Chapter 7, the obtained results are discussed and the comparison of different PK models is covered.

# **Chapter 2**

## **The blood filter**

There is no life without metabolizing, and metabolism always produces variety of waste products, which accumulated in the tissues are toxic to the organism. Some of them are removed from the body by respiratory tracts, others through digestive system and some of them are extracted through the sweat glands. However, there is no doubt that the urinary system plays the major role in waste extraction [2, 10].

The main organs of the urinary system are the kidneys. It is them, which perform the filtering function. The remaining ones, ureters, urinary bladder, and urethra, form the urinary tracts and are responsible only for transforming and storing the urine [2]. In this chapter the anatomy and physiology of the kidneys will be briefly introduced.

### **2.1 Structure of the kidney**

The kidneys are bean-shaped, usually paired structures located at the back of the abdominal cavity in the retroperitoneal space. They lie at the level of vertebrae T12 to L3. The right kidney is slightly lower than the left one, because of the close

proximity to the liver [2, 10].

The average healthy adult kidney weights around 150 g, is 11 cm long, 6 cm wide and 3 cm thick [2, 11]. As mentioned before, humans usually have two kidneys, however not always. Some people are born with only one of them. In such case, the present kidney is as heavy and big as the two kidneys together would be. In most cases it doesn't affect normal live [12].

The kidneys are surrounded and protected by three types of connective tissue, from the outer part: (1) *renal fascia* anchoring the kidneys and the neighbouring organs to the abdominal wall; (2) *adipose capsule*, which is a layer of fat tissue holding the kidney in place; (3) *renal capsule*, made of fibrous tissue, firmly enclosing the organ and protecting it from traumas and infections [2, 10]. In the medial concave surface, there is a slit called *hilum*, which is the place where the renal artery enters and the renal vein and the ureter leave the kidney. The hilum extends into the *renal sinus*, which is a large cavity occupied by blood and lymphatic vessels, nerves, urine-collecting structures and adipose tissue [10].

The renal parenchyma is divided into two major parts: (1) the outer 1 cm thick portion of the kidney, *renal cortex* (2) the inner *renal medulla* [2, 10]. The cortex projects into the kidney forming *renal columns*, which divide the medulla into 10–14 *renal pyramids*. Each of them has a characteristic shape of a cone with the wide base facing the cortex and the tip attached to the sinus called *renal papilla*. The papilla of each pyramid points towards the *minor calyx* collecting its urine. Few of them converge into the *major calyx*, whereas the all latter ones form the funnel-shaped basin, the *renal pelvis*, which is the extension of the *ureter* transforming the urine to the bladder [2, 10, 13]. The gross anatomy of the kidney is illustrated in Figure 2.1.

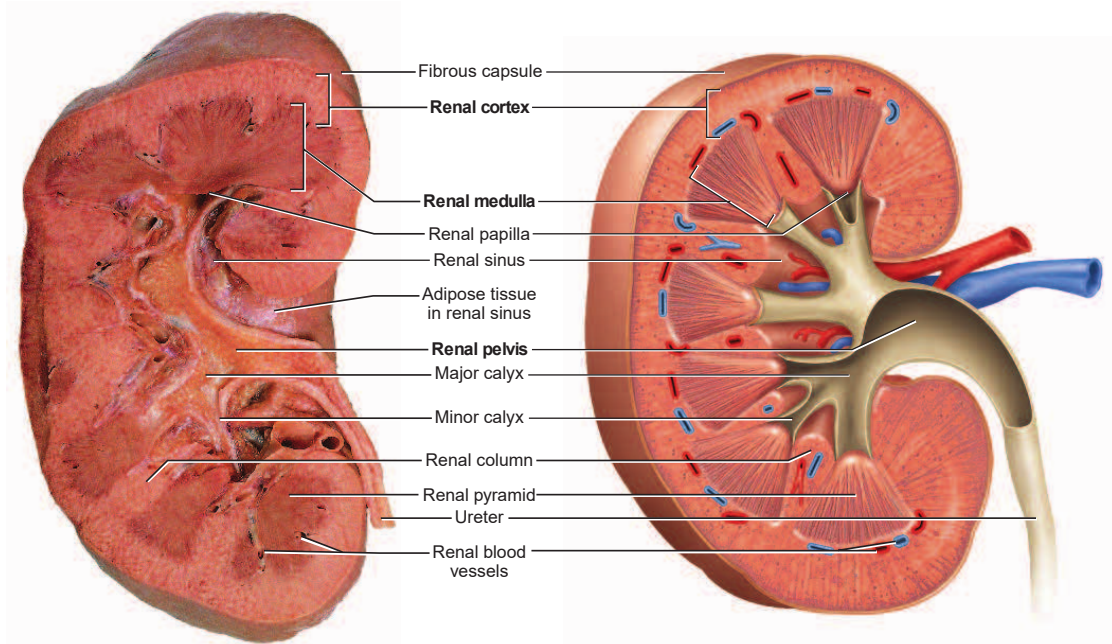


**Figure 2.1.** Gross anatomy of the kidney [2].

### 2.1.1 The nephron

As it is with most of the aspects of the human anatomy, the most interesting features of the kidney are invisible with naked-eye. The basic microscopic functional units of the kidney are *nephrons*. Above million of them enables the kidney to perform its functions [10]. Each of them is a tiny coiled tube, called the *renal tubule*, with a bulb at the end, the *renal corpuscle*, and extends through both the cortex and the medulla [2].

The renal corpuscle is composed of the two-layered *glomerular (Bowman) capsule* enclosing the *glomerulus*, which is a cluster of capillaries. The renal tubule is a duct leading from the glomerular capsule to the pyramid papilla. It can be divided into several regions, subsequently from the glomerular corpuscle: (1) the *proximal convoluted tubule* (PCT); (2) the *nephron loop (loop of Henle)*, which consists of the *descending and ascending limbs*; (3) the *distal convoluted tubule* (DCT); (4) the *collecting duct*.

*duct* receiving the fluids from the DCTs of few nephrons. Multiple of the collecting ducts merge and form a papillary duct, which lead to the minor calyx. Each of the segment has a distinct cellular appearance and function [2, 10, 13].

Every functional unit of the kidney is supplied with the blood by a small blood vessel called the *afferent arteriole*, whereas the *efferent arteriole* takes it back. The blood leaving the nephron, flows into a network of *peritubular capillaries* surrounding the renal tubule [2, 10]. The particular parts of the nephron are depicted in Figure 2.2.

## 2.2 Functions of the kidney

Despite the fact that the key function of the kidneys is purifying the blood, the other ones are equally important. Kidneys are responsible for maintaining the homeostasis of the whole body due to which, all organs can work in an optimal environment. It is crucial for a proper functioning of whole organism [13]. One can conclude that the role of kidneys is enormously important. Indeed, the kidneys are involved in the following processes:

**Blood filtering.** The kidneys filter the blood from metabolic waste, excessive amounts of salts, toxins and then excrete unwanted substances in the urine [2, 10, 13].

**Osmoregulation.** For a proper functioning of the organism, the concentration of the salts in the body has to remain relatively the same. The kidneys influence this concentration by controlling the amount of water and solutes excreted from the organism [14].

**Maintenance of water balance.** The kidneys control the amount of water conserved and eliminated in the urine so that the amount of body water remains on the stable level [15].

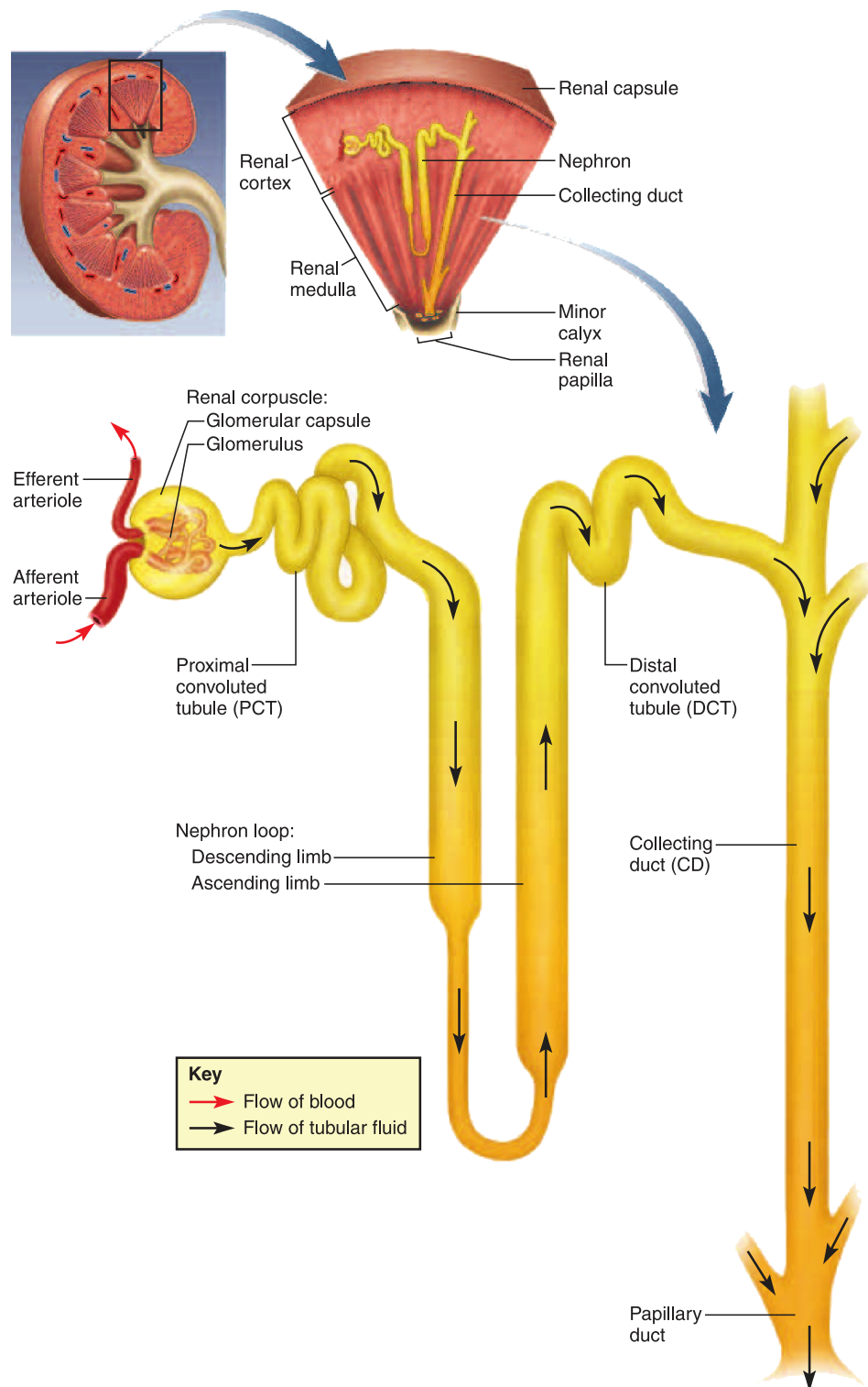


**Figure 2.2.** The structure of the nephron [2].

**Blood pressure regulation.** Maintaining the normal blood pressure is achieved in two ways: (1) if the blood pressure drops, the kidneys release the enzyme *renin*, which activates the blood protein *angiotensin*, making the blood vessels to constrict. What is more, angiotensin triggers the mechanism which increases the absorption of water and sodium, which in turn increase the blood volume; (2) by regulating the amount of water, which was mentioned before [16].

**Maintenance of the acid-base balance.** The food contained in our diet can acidify or alkalize the organism. If the pH level is out of the tolerable boundaries, enzymes and proteins break down, which in extreme cases can lead to death. Kidneys in collaboration with the lungs are responsible for maintaining healthy pH of the body fluids. While the lungs' task is to regulate carbon dioxide ( $CO_2$ ) concentration, the kidney acts by reabsorbing or regenerating bicarbonate ( $HCO_3^-$ ) from the urine and excreting hydrogen ions and fixed acids into the urine [17].

**Red blood cell production.** If the level of oxygen in the tissues is insufficient, the kidneys release *erythropoietin*, the hormone stimulating the bone narrow to red blood cells production [18].

**Keeping the bones strong.** The kidneys, together with the liver, synthesize the active form of vitamin D called *calcitriol* (1,25-dihydroxycholecalciferol) enabling the body to absorb calcium and phosphorus, which are the crucial minerals for strengthening the bones [19].

**Prevent the hunger.** In the situation of extreme starvation, the kidneys can synthesize glucose from non-carbohydrate carbon substrates, breaking down other molecules. This phenomena is known as *gluconeogenesis* [20].

### 2.2.1 Urine formation

Everyday our kidney filter as much as 200 litres of fluid, which is 60 times volume of blood in the body, and excrete 1.5 litres of urine [2]. These enormous amounts are a result of complex process involving numerous exchanges between a nephron and the blood stream. The process of the urine formation can be divided into 4 stages:

1. **Glomerular filtration.** When the blood enters the glomerulus through the afferent arteriole, the first step begins. Sieve-like walls of the glomerular capillaries pass every molecule smaller than 3 nm to the glomerular capsule. These molecules include the water and some solutes as glucose, electrolytes, fatty acids, nitrogenous wastes, amino acids and vitamins. On the other hand, they are impermeable to the larger components such as protein molecules and blood cells. The diameter of the afferent arteriole is larger than that of efferent one, which gives the capillaries a large inlet and a small outlet. This in turn causes the pressure in the glomerulus to be much higher than elsewhere in the organism. Because the high pressure overrides the reabsorption, the movement of the particles occurs. This movement of the components, from the blood into the Bowman's capsule is known as *glomerular filtration* and the fluid in the glomerular capsule, *glomerular filtrate* [2, 10].
2. **Tubular reabsorption.** The filtrate passing through the renal tubule apart from wastes, contains also water and many other useful substances such as ions and nutrients, which is a huge loss to the organism. Thus, they are being regained and returned to the bloodstream during the *tubular reabsorption*. The movement is not direct but involves also extracellular fluids and is obtained through the *diffusion, osmosis* and *active transport* [10].
3. **Tubular secretion.** At this stage the final adjustment of the content of the urine is made. Wastes, toxins and unnecessary substances are passed from the

blood to the renal tubule. What is of great importance, in this process also the hydrogen and bicarbonate ions can be removed in order to regulate the acid-base balance of the body [10].

4. **Urine condensation.** When the filtrate enters the collecting duct, it becomes the urine. In order to prevent the water loss and keep the fluid balance of the body, during the last step the water is returned to the tissue fluid and the bloodstream, which makes the urine more and more concentrated [2].

The urine formulated in such a way is then extracted from the organism. The above stages are summarized in Figure 2.3.

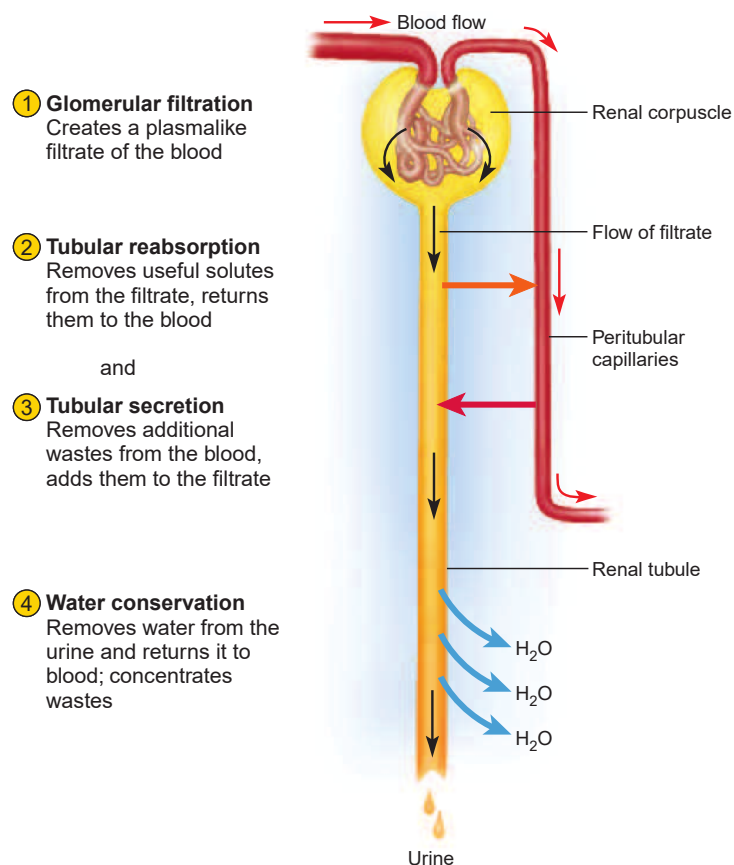


**Figure 2.3.** Process of the urine formation [2].

## 2.2.2 Glomerular filtration rate

*Glomerular filtration rate* (GFR) is a volume of fluid filtered during glomerular filtration from the renal glomerular capillaries into the Bowman's capsule per unit time by two kidneys combined and its unit is mL/min [21]. After standardisation, which is recalculation for standard *body surface area* (BSA), GFR is expressed in mL/min/1.73 m<sup>2</sup> [2].

The GFR in healthy adult kidneys is equal to approx. 90–130 mL/min/1.73 m<sup>2</sup> [22]. Lower at birth, it approaches its adult value at the age of two and maintains its level till the age of forty, when it starts decreasing again [23]. Proper GFR value determines performance of several basic functions of the kidney. Neither too low, nor too high GFR is healthy to the organism [2].

In clinical practice, GFR is an approximate estimator of the number of active nephrons and is considered as a unit of level of kidney function. What is of great importance, GFR can also determine the stage of chronic kidney disease [6]. GFR between 60–120 mL/min/1.73 m<sup>2</sup> is considered a normal, healthy value, below 60 mL/min/1.73 m<sup>2</sup> indicates definite kidney disease, while the number under 15 mL/min/1.73 m<sup>2</sup> is associated with renal failure [24]. The reference values of GFR are shown in Figure 2.4.

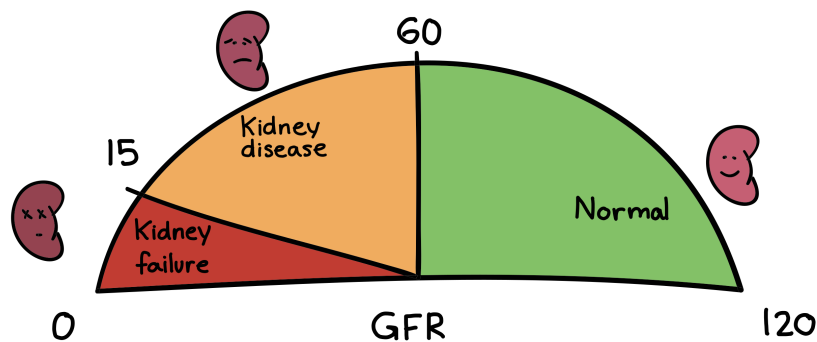


Figure 2.4. GFR reference values [25].

Due to the fact that the concentration of the particular substance in the blood and the urine is influenced not only by glomerular filtration, but also by tubular reabsorption and secretion, GFR cannot be measured directly by comparing the urine and blood concentrations. In this way one would rather obtain *renal clearance*, which is a volume of blood plasma from which a particular waste is completely removed in a unit time [2]. This dependency is expressed as follows:

$$\frac{\text{glomerular filtration of the waste}}{\begin{array}{l} - \text{ tubular reabsorption of the waste} \\ + \text{ tubular secretion of the waste} \end{array}} = \text{renal clearance} \quad (2.1)$$

For that reason, GFR measurement requires a substance that is neither secreted nor reabsorbed by the nephrons, which implies that its entire amount in the urine is passed there by glomerular filtration. Unfortunately, there is no single solute appearing in the urine and naturally produced by the body, which doesn't undergo the tubular secretion or reabsorption to some degree [7].

However, in the nature there appear a substance, which accomplishes the above conditions, namely *inulin*. One method of accurate measurement of glomerular filtration rate incorporates injecting inulin and subsequently measuring the rate of urine output and the concentrations of inulin in the blood and urine. For inulin, the GFR is equal to the renal clearance [2, 7].

Even though this method is considered the gold standard in the GFR measurement, due to its limitations it is not a clinical routine unless very accurate measurements are required. This special cases include transplant donors or scientific research [6]. Other, more frequently used techniques involve using endogenous markers such as *creatinine* and estimating GFR by applying validated algorithms [7].

# Chapter 3

## Dynamic contrast enhanced MRI

Medical Imaging started with the development of X-rays by Wilhelm Röntgen in 1895, for which he received a Nobel Price [26]. An enormous progress has been done since that time and numerous different imaging methods were developed, which found various applications in the medical field. Possibility of creating the visual representations of human interior as well as the processes occurring in tissues and organs, and thus their functionality, much facilitated medical diagnosis and prognosis. Some imaging techniques have became an integral part of clinical care (i.e. computer tomography, magnetic resonance imaging, positron emission tomography, etc.), whereas there exist one, which still needs to prove its utility.

In this chapter the imaging technique, which is DCE-MRI will be introduced and its mechanism of imaging will be presented.

### 3.1 Fundamentals of MRI

In order to understand the mechanism of acquiring DCE-MRI sequences, it is inevitable to introduce the principle of operation of *magnetic resonance imaging* (MRI).

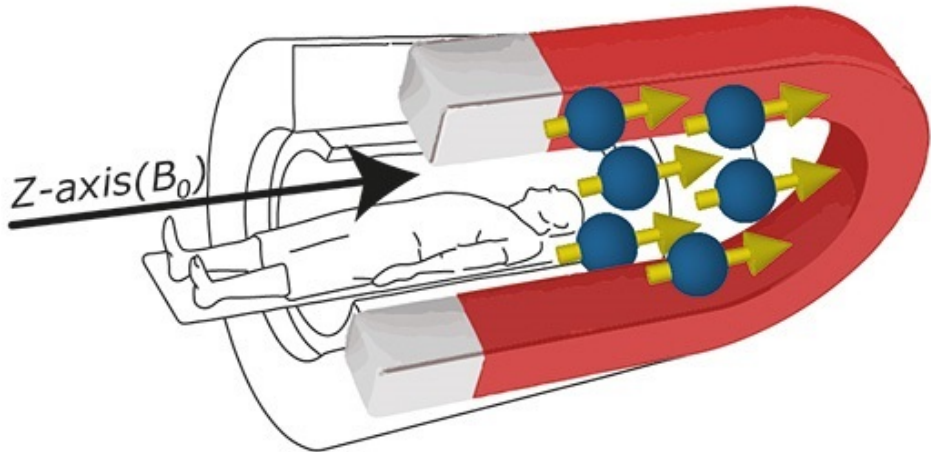


**Figure 3.1.** Hydrogen atoms located in a human body placed in the strong magnetic field ( $B_0$ ) generated by the MRI scanner align to the direction of that field [31]. Note that this image is for visualisation of the idea only and it may not present the actual structure of the MRI scanner.

MRI is an imaging technique based on the phenomena of induced nuclear magnetism in the patient. Every molecule possessing a nuclei with an odd number of protons or neutrons have a spin, implying a weak though observable randomly oriented nuclear magnetic moment. These particles include for example  $^1\text{H}$ ,  $^{13}\text{C}$ ,  $^{31}\text{P}$ ,  $^{23}\text{Na}$ ,  $^{19}\text{F}$  [28, 29]. If placed in a strong static magnetic field, these moments strongly tend to align parallel to the external field. Some of them will align antiparallel to the field, however there will always be an excess of these directed towards the direction of the field, as this state is more energetically stable. The resulting net magnetic moment,  $M_0$ , will be directed with the external field [30].

Magnetic resonance imaging exploits the fact that the human body in 80% consists of water. During the MRI examination, the object is placed in the scanner producing a strong magnetic field, which causes the hydrogen atoms to align in the direction of the field, pointing towards the head of the object as shown in Figure 3.1 [30].

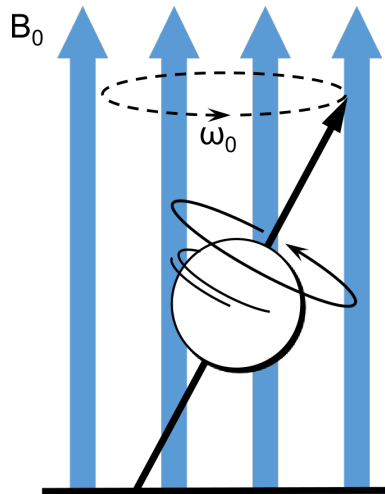


**Figure 3.2.** Hydrogen atom placed in a strong magnetic field  $B_0$  precesses about the direction of that field with the frequency  $\omega_0$ . On the basis of [30].

In addition, atoms have an angular momentum making them precess about the magnetic field direction with a frequency  $\omega_0$ , called the *Larmor frequency*, which is proportional to the field:

$$\omega_0 = \gamma B_0 , \quad (3.1)$$

where  $\gamma$  is the nuclei specific constant *gyromagnetic ratio* (for hydrogen equal to 42.6 MHz/T) and  $B_0$  is the strength of the external magnetic field [28, 30]. This precessional motion is shown in Figure 3.2.

Further, when the *radio-frequency* (RF) pulse equal to the Larmor frequency is applied perpendicularly to the magnetic field, the resonance occurs. The atoms absorb the energy, transits to the higher energy state and flip to other position. When the RF transmission is stopped, the atoms return to their equilibrium state (realign to the field  $B_0$ ) releasing the energy as a radiation signal, referred to as a *free-induction decay* (FID) response signal, which is picked by the MRI receiver. This return to equilibrium is called *relaxation*. The relaxation time as well as the amount of the energy released strongly depends on the magnetic properties of the tissue, which means that every tissue generates different response signal.

The dedicated software analyses and processes obtained signal, which is a combination of numerous response signals from all excited atoms and generates the image [28, 30].

During the MRI examination, the strength of the magnetic field produced by the scanner varies along the body, so that the Larmor frequency is different for different regions. By changing frequency of emitted RF, the appropriate part can be imaged.

The typical MRI scanner consists of:

1. **The main field magnets**, which produce strong, uniform magnetic field polarizing the sample [28]. Typical strength of the field of a clinical MRI scanner ranges between 0.2–1.5 T, whereas research systems reaches values even up to 21 T for animal models [29, 32].
2. **Shim coils**. In clinical practice, the main field magnets never produce perfectly uniform field so the shim coils adjusting its homogeneity have to be used [28].
3. **Gradient coils** producing three secondary gradient magnetic fields in each of the  $x$ -,  $y$ - and  $z$ - direction. In this way, the resonance frequency of protons varies as a function of position, which enables encoding the spatial position and imaging of thin anatomic slices [33].
4. **RF system**, task of which is to excite the hydrogen atoms and to receive their FID response signal [28].
5. **The processing unit of high performance** controlling the system and processing the received combination of response signals [28].

### 3.1.1 $T_1$ - and $T_2$ -weighted images

Although there are few approaches of obtaining the contrast between different tissues in an image, utilizing different tissue properties, most widely used in clinical

applications are those based on the relaxation of the magnetization. However, there are two kinds of relaxation, and thus two mechanisms of creating the MRI image can be distinguished [28].

**$T_1$ -weighted images** exploits spin-lattice relaxation, characterised by the time  $T_1$ , which describes the time required by excited atoms to return to the equilibrium state after it was altered by the RF pulse. This mechanism is shown in Figure 3.3a. Sometimes the acquiring of  $T_1$ -weighted sequence is preceded by the injection of *gadolinium* (Gd), a paramagnetic *contrast agent* (CA), which shortens time  $T_1$  and appears very bright in the image. This property is especially useful while visualising vascular structures or brain tumours and abscesses blocking a blood supply [28, 29].

**$T_2$ -weighted images** are based on spin-to-spin relaxation, described by the  $T_2$  indicating the time required by the nuclei response signal to decay after it has been created [28, 29].  $T_2$  contrast is presented in Figure 3.3b.

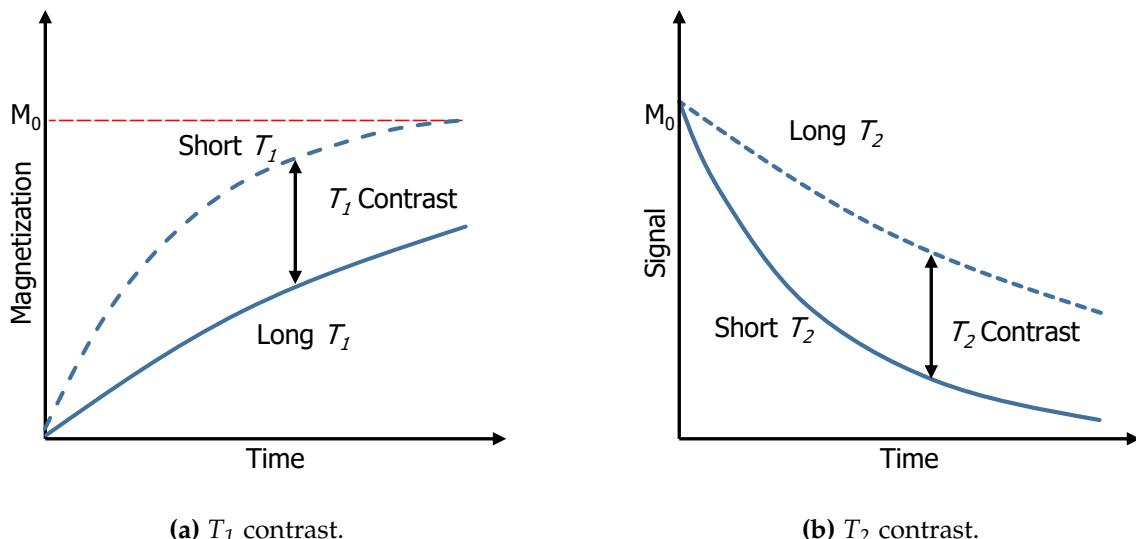
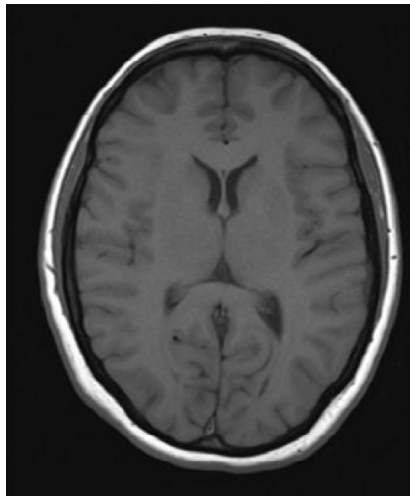
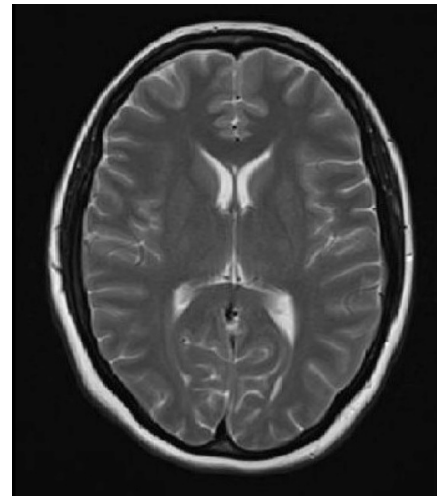


**Figure 3.3.**  $T_1$  and  $T_2$  contrast mechanisms [28].



(a)  $T_1$ -weighted image of a brain.



(b)  $T_2$ -weighted image of a brain.

**Figure 3.4.** Example MRI image of a brain of a healthy volunteer demonstrating  $T_1$  and  $T_2$  contrast [34].

Examples of the images acquired using described above two basic mechanisms are shown in Figure 3.4a-b. The figure presents identical axial section of a healthy person's brain. In the  $T_1$  weighted image, one can notice ring of subcutaneous fat, which is bright due to its short spin-lattice relaxation time. Gray matter has longer  $T_1$  than white matter, so it appears darker. In the second picture, utilizing the  $T_2$  difference between tissues, cerebrospinal fluid in the ventricles appears very bright due to its long  $T_2$ .  $T_2$  of the white matter is shorter than those of gray matter, which makes the latter one brighter.  $T_1$  and  $T_2$  weighted images are only two of the few contrast mechanisms used in MRI and the choice of appropriate one strongly depends on the application and the *region of interest* (ROI) under examination [28].

Currently, MRI is one of the most widely used medical imaging techniques applied to all parts of a body. It allows to create the detailed anatomical images in axial, sagittal, coronal or even oblique plane. During the MRI examination subsequent thin 2D *slices* along chosen axis are produced, which makes it a tomographic

imaging method. As a result, during imaging sequence, a large dataset is acquired, from which any anatomical section can be reconstructed or a 3D model of a ROI can be assembled [30]. Another advantage of MRI is not using any harmful ionizing radiation.

The clinical applications of MRI include diagnosis of blood vessel damages, multiple sclerosis, brain injuries, spinal cord injuries, brain strokes, blocked blood vessels, heart diseases, damages caused by a heart attack, bone infections, different kind of tumors and cancers and many more [35].

## 3.2 Fundamentals of dynamic contrast enhanced MRI

*Dynamic contrast enhanced magnetic resonance imaging* boils down to the acquisition of multiple MRI scans, with addition of one significant component—the time domain [36]. During the examination a contrast agent is injected in the peripheral vein into the bloodstream, and the  $T_1$ -weighted images are acquired with fast imaging technique. The passage of the tracer through the target tissue results in changes in signal intensities over the time. The kinetics of the CA, so its temporal and spatial distribution is strongly dependent on the physiological parameters such as tissue perfusion, volume of the extravascular and extracellular space and vessel permeability, and thus the analysis of so obtained intensity changes as a function of time,  $S(t)$ , provides important functional information [8, 9]. As an example, malignant tumours show faster and higher levels of enhancement than normally functioning tissue, which is associated with tumour's increased vascularity and higher endothelial permeability to the CA [36].

### 3.2.1 DCE-MRI analysis

There are many methods of time courses analysis obtained during DCE-MRI. In general, they can be divided into qualitative, semi-quantitative and quantitative [37]. All methods can be applied voxel-wise or to the whole region of interest, where the average time-intensity curve is produced from the voxels values within the ROI [9].

#### 3.2.1.1 Qualitative analysis

In a traditional approach, the evaluation of the time-intensity curves is performed by an experienced observer via subjective visual inspection, who's task is to classify the curve to one of the three predefined enhancement patterns. These three templates are shown in Figure 3.5.

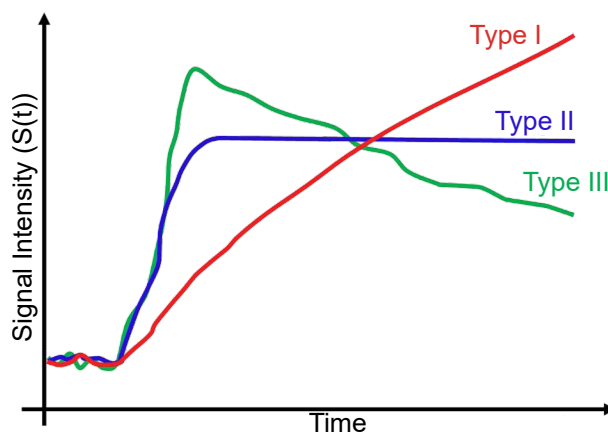


**Figure 3.5.** Different DCE-MRI enhancement patterns [9].

Type I defines a shape characterized by the gradual increase of the signal intensity during the whole acquisition time. In type II, after the initial peak, the plateau occurs—the curve remains relatively constant. Type III is associated with the decrease in signal intensity after the peak signal intensity [37]. In this way, i.e. the tumour can be distinguished from the healthy tissue.

Although the qualitative analysis is a very convenient one as it does not require any additional data and calculation, its major disadvantage is not delivering any quantitative parameters and being fully dependent on the observer's experience.

### 3.2.1.2 Semi-quantitative analysis

The semi-quantitative analysis incorporates calculation of parameters directly from the time-intensity curve characterizing its shape [9, 37]. Several examples of the parameters include *onset time* ( $T_o$ ), *maximum signal intensity* ( $S_m$ ), *peak enhancement* ( $\Delta S$ ), *time to peak* ( $T_p$ ), *wash-in slope*, *wash out slope*, *average plateau*, *area under the curve* (AUC) or *initial area under the uptake curve* (IAUC) [9]. Listed parameters are depicted in Figure 3.6.

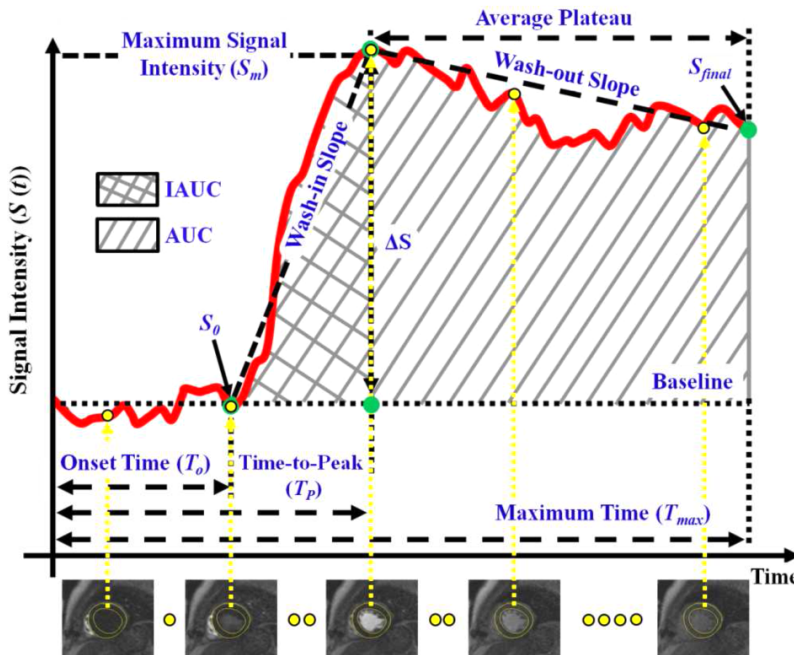


**Figure 3.6.** An example of the time-intensity curve,  $S(t)$ , with depicted metrics explored in semi-quantitative DCE-MRI analysis. Note that  $S_0$  is the signal intensity before CA arrival whereas  $S_{final}$  is the intensity registered in the last temporal point at the end of the experiment  $T_{max}$  [9].

As in the case of previous method, the ease of the calculations performed directly from the curve is its biggest advantage. However, the obtained empirical parameters in some way correlate with tissue physiology, i.e. increased vascular density or permeability usually increases the wash-in slope, AUC, and peak enhancement, in the same time decreasing the time to peak, it is difficult to relate them directly to some particular physiological quantities [37].

### **3.2.1.3 Quantitative analysis**

Quantitative assessment of the  $S(t)$  curve is surely the most sophisticated one. It involves fitting one of the several quantitative mathematical models, which describes the pharmacokinetics of the CA to the concentration-time curve of the target tissue. Not only does this type of analysis require acquisition of the intensity-time curve of the feeding blood vessel next to that of the target tissue, but also one has to convert the obtained curves into CA concentration-time curves. In reward, some physiologically interpretable kinetic parameters of the tissue are estimated [36, 37]. The issue of the pharmacokinetic modelling in details is described in Chapter 4.

## **3.2.2 DCE-MRI applications**

Even though not present in clinical routine yet, over the last two decades DCE-MRI has been widely explored in clinical studies. There is no doubt that obtaining important functional information next to the anatomical one in a single imaging session is one of the biggest advantage of dynamic contrast enhanced MRI. It has shown to have a great potential in early detection of breast cancer, providing higher sensitivity than classical mammography, as well as detection of small lesions, which classical MRI is not capable to. What is more, it showed promising results in accurate localisation of prostate cancer. Further, DCE-MRI was found to be

a reliable technique of monitoring tumour responses for treatment (changes in vascular support). DCE-MRI also showed its effectiveness in accurate detection of renal rejection. Last but not least, what is of great importance for this project, from the DCE-MRI images, important physiological parameters of the tissue, such as GFR of the kidney can be estimated [9].

The mentioned findings, which are only a drop in the ocean of researches, suggest that DCE-MRI is a relevant non-invasive imaging technique, which can be a part of clinical care used in a really wide range of applications.

# Chapter 4

## Pharmacokinetic modelling

The ideal output obtained from DCE-MRI analysis would be some reliable quantitative physiological parameters of the tissue under examination. Numerical results, however, always call for some mathematical description of the system under examination.

The time-dependent distribution and deposition of a substance in a living system can be described by *pharmacokinetic* (PK) models [38]. First attempts of depicting the organism by a set of components were performed by Torsten Teorell in 1937. He then created a model of whole body shown in Figure 4.1 and described the processes inside by a set of differential equations in the same time presenting their solutions [39]. Teorell is now considered a father of pharmacokinetic modelling.

PK models aim to characterise a physiologic system, not necessarily the whole body, by decomposing it into interacting compartments. Every of them is a homogenous, well-mixed space with the uniform tracer distribution [40]. Thus, the multi-compartment system reaches the equilibrium at different time. PK models have a very wide clinical application: from estimating the optimal drug dose to determining safe working environment while working with toxins [38].

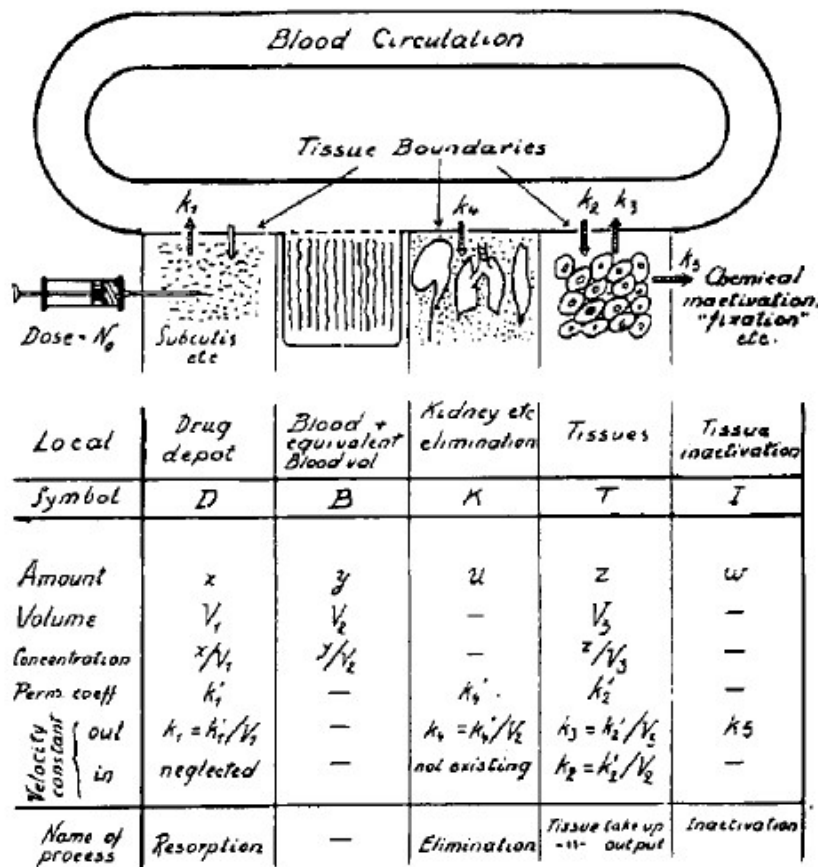


Figure 4.1. First PK model described by Teorell [39].

Given the fact that the CA used in DCE-MRI examination can be considered as a substance flowing through the organism, pharmacokinetic modelling can also be used in analysis of so obtained data. This approach, called the quantitative one, is based on fitting a mathematical model to acquired tissue concentration time courses [9, 36, 37]. In this way, the quantitative parameters can be assessed, which cannot be overestimated while evaluating the tissue function.

This chapter deals with the approach of PK modelling giving the brief inside in its basic principles and requirements with focus on DCE-MRI applications.

## 4.1 The tracer kinetic theory

The compartment PK models describe complex blood-tissue exchanges. The general tracer kinetic theory is based on principle of mass conservation and PK models are formulated as mass balance equations [9, 41].

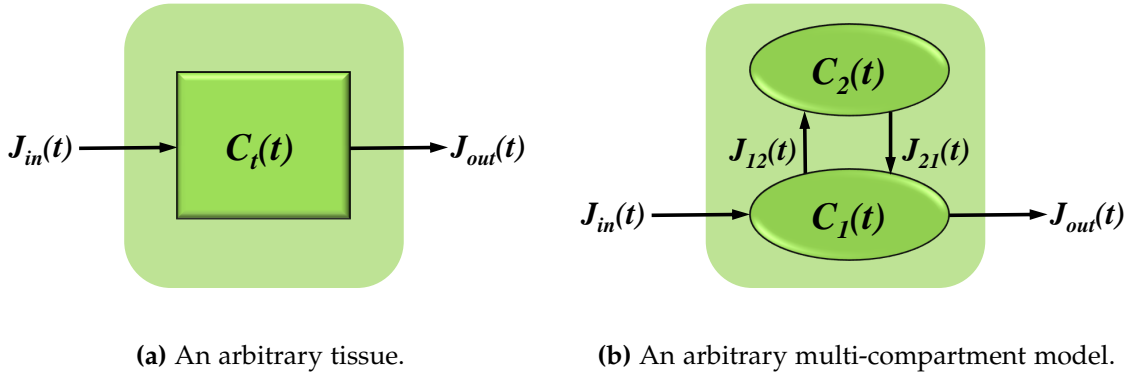


**Figure 4.2.** An arbitrary tissue with a possible compartmental architecture. The system (square) has one inlet and one outlet. The tracer in the volume of distribution is indicated in dark green in (a).  $J_{12}$  and  $J_{21}$  are fluxes between compartments (oval shaped).

Given the tissue with at least one inlet and one outlet (see Figure 4.2a), the time-varying tracer concentration in the tissue,  $C_t(t)$  can be expressed as [41]:

$$C_t(t) = \frac{M_t(t)}{V_t}, \quad (4.1)$$

where  $M_t(t)$  is the amount of tracer in the tissue [mmol] and  $V_t$  is the volume of the tissue [mL]. The *flux* [mmol/mL/min] in terms, is the amount of the tracer, which travels through an inlet or outlet per unit time. After the normalisation to the unit tissue volume the flux can be expressed as [41]:

$$J(t) = \frac{1}{V_t} \frac{\partial M_t(t)}{\partial t} \quad (4.2)$$

Let's now consider an arbitrary multi-compartment model composed of  $n$  interacting compartments. Then, the outlet of one compartment is in the same time the inlet of another, see Figure 4.2b. The tissue concentration in such a system is defined as [41]:

$$C_t(t) = \sum_{j=1}^n v_j C_j(t), \quad (4.3)$$

where  $v_j \leq 1$  is the *fractional volume* [dimensionless] of  $j$ th compartment and  $C_j$  is the concentration of tracer in this compartment. From the principle of the conservation of the mass it is known that no amount of the indicator is neither created nor destroyed in the tissue. Under such condition, applying the mass balance equation to the every of the compartments, the change of the total amount of substance in the compartment is given by [41]:

$$\frac{dM_j(t)}{dt} = \sum_{i \in \text{Inlets}} \frac{M_i(t)}{\partial t} - \sum_{o \in \text{Outlets}} \frac{M_o(t)}{\partial t} \quad (4.4)$$

After normalisation to the unit tissue volume [41]:

$$v_j \frac{dC_j(t)}{dt} = \sum_{i \in \text{Inlets}} J_i(t) - \sum_{o \in \text{Outlets}} J_o(t), \quad (4.5)$$

The mass conservation principle implies that the amount of the substance transported from a compartment  $i$  to a compartment  $j$  per unit time is equal to the amount of the given substance leaving the  $i$ . This leads to the formula [41]:

$$\frac{\partial M_{ij}(t)}{\partial t} = k_{ep} M_i, \quad (4.6)$$

where  $k_{ep}$  is so-called *rate constant* [ $\text{min}^{-1}$ ]. Again, after the normalisation to the unit tissue volume [41]:

$$J_{ij}(t) = K_{trans} C_i(t), \quad (4.7)$$

where  $K_{trans} = k_{ep}v_j$  is *transfer constant* [ $\text{min}^{-1}$ ].  $K_{trans}$  combines both the flow and tissue permeability. Some approaches allow for their separate estimation by differentiating the *flow F* by the *permeability surface area product, PS* [41].

#### 4.1.1 Linear stationary systems

All PK models are based on two fundamental assumptions, without which solving the models' equations would not be possible: that the system is linear and stationary. Hence the response of the influx is proportional to the dose of the injected tracer [41, 42].

For any linear and stationary system satisfying the initial condition  $C_t(0) = 0$ , which means  $t = 0$  is chosen before tracer injection, the tissue concentration can be obtained by convolving the concentration of tracer input function with the *impulse response function* (IRF) of the tissue denoted as  $h(t)$  [42]:

$$C_t(t) = C_{in}(t) \circledast h(t) = \int_0^t C_{in}(\tau)h(t - \tau)d\tau \quad (4.8)$$

When the only inlet of the examined tissue is an artery, the input function corresponds to the function of plasma concentration at the entrance of the system and can be derived from so-called *arterial input function* (AIF),  $C_{in} = C_p$ . The IRF in terms can be found by applying the Laplace transform to the appropriate mass balance equations [41].

#### 4.1.2 One-compartment model

For better understanding, the above theory will be explained on an example one-compartment model, but the reasoning is similar for all models used in this work. Given an one-compartment system with a single inlet and outlet and taking into consideration that all substances in the system have constant volume, it is known that inflow have to level the outflow. On the basis of Formulas (4.5), (4.7) the mass balance equation of the system can be formulated as follows [41]:

$$v_1 \frac{dC_1(t)}{dt} = K_{trans}(C_{in}(t) - C_1(t)), \quad (4.9)$$

where the  $v_1$  is the fractional volume of the compartment. From Formula (4.3) [41]:

$$\frac{dC_t(t)}{dt} = K_{trans}(C_{in}(t) - C_t(t)/v_1) \quad (4.10)$$

Assuming that  $C_{in}$  is a short pulse of concentration,  $C_{in} = \delta(t)$ , the IRF of the tissue can be obtained by applying the Laplace transform to Formula (4.10):

$$\mathcal{L}\{\dot{h}\}(s) = K_{trans}(\mathcal{L}\{\delta\}(s)) - \frac{K_{trans}}{v_1}(\mathcal{L}\{h\}(s)) \quad (4.11)$$

Making use of the properties of the Laplace transform, the solution is [41]:

$$h(t) = K_{trans}e^{-k_{ep}t} \quad (4.12)$$

Finally, according to Formula (4.8), the tracer concentration in the tissue can be expressed as [41]:

$$C_t(t) = C_{in}(t) \circledast K_{trans}e^{-k_{ep}t} \quad (4.13)$$

The physical and mathematical background described above was shortened so that to introduce very basics and explain enough but not too much on the theory of

PK models. If interested, the reader is kindly referred to the original sources [41, 42].

There exist numerous PK compartment models used in DCE-MRI analysis and each of them is based on different assumptions and simplifications, which are not proper in all cases. The choice of the model depends on such factors as a type of a tissue under consideration, the quality of input data, the possibility of obtaining the AIF and many more [9]. One should, however, remember that no mathematical equations will ever describe the living organism accurately in 100% as there are no two samples of tissue behaving exactly in the same way. The most widely used PK models include: *Tofts and Kermode* (TK) [43], *extended TK* (ETK) [44], *two-compartment Exchange* (2CXM) [9] and *Patlak-Rutland* (PR) [45] models.

## 4.2 Arterial Input Function

The quantitative approaches of DCE-MRI analysis require obtaining the input function delivering the tracer to the system. From the physiological point of view, the tracer is delivered to the tissue of interest through the feeding blood vessels, so the input function becomes the plasma concentration,  $C_p$  in these vessels. Plasma concentration can be obtained from so-called *arterial input function* (AIF), which describes the changes of the tracer concentration in the feeding blood source. Its tracer kinetics differs significantly from this of the tissue. The changes in plasma concentration are fast and sharp and it is of great importance to cover the rapid peak of the signal or else the important information about the tissue are lost [9, 36, 37]. In general there are three approaches of acquiring the AIF:

1. **Gold standard AIF** is obtained by blood sampling during DCE-MRI examination. Although its accuracy strongly depends on the frequency of collected samples, this method usually allows for accurate measurement of the AIF, but is inconvenient for both the patient and the examiner. What is more, in some

cases, for example during DCE-MRI of a breast, blood collection close to the tissue of interest is impossible to perform due to the lack of big vessels in this region [9, 37].

2. **DCE-MRI AIF** is determined directly from the obtained DCE-MRI data. In this approach the time-varying signal intensity from the region containing large feeding artery is converted into the tracer concentration in this way estimating the AIF. The major limitation is that it is not always possible to cover the desired artery in the DCE-MRI acquisition field, for example during imaging small lesions in a breast [9].
3. **Population-based AIF** is obtained by averaging the AIF of the group of subjects to be used in subsequent studies of the similar subjects. Because the need of acquiring subject-specific AIF is eliminated, the temporal resolution of the DCE-MRI can be decreased (CA tissue kinetics is slower than in the blood) in the same time increasing the quality of the images or the spatial resolution. The biggest disadvantage of this method is possible variance between individual AIFs [36].

### 4.3 Intensity to concentration conversion

Because the PK models describe kinetics of the system in terms of the CA concentration in the tissue and the output of DCE-MRI examination is the signal intensity as a function of time, the conversion of the signal intensity to concentration is indispensable. As long as the relationship between CA concentration and the signal intensity is linear, and the same for both the tissue and the blood in case of acquiring AIF from DCE-MRI images, the conversion boils down to the subtracting the baseline so that the concentration before the tracer arrival is at the level of 0.

These conditions are satisfied at low doses of CA [9]. At high doses of the CA, however, this linearity is not true anymore due to the saturation effect of the signal. Non-linearity adds one more complication to the DCE-MRI examination. In such case, in order to convert the signal intensity into the CA concentration, the maps of the native relaxation time,  $T_{10}$ , which is the value of  $T_1$  before the tracer injection, have to be measured. Then, the values can be substituted to Formulas (4.14), (4.15) and the CA concentration can be obtained [9, 36, 37].

The dependency between the CA concentration in the tissue,  $C_t(t)$ , and the relaxation rate,  $1/T_1(t)$ , is given by the Solomon-Bloembergen equation [36]:

$$\frac{1}{T_1(t)} = \frac{1}{T_{10}} + r_1 C_t(t), \quad (4.14)$$

where  $r_1$  is the spin-lattice relaxation constant depending on temperature, field strength and the chemical structure of the tracer. On the other hand, under certain assumptions, the magnitude of the signal during the standard DCE-MRI can be predicted by [9, 36]:

$$S(t) = M_0 \frac{\sin \alpha (1 - e^{-TR/T_1(t)})}{1 - (\cos \alpha) e^{-TR/T_1(t)}}, \quad (4.15)$$

where  $M_0$  is a scaling constant dependent i.e. on the scanner parameters and the proton density,  $TR$  is the repetition time,  $T_1$  is spin-lattice and relaxation time and  $\alpha$  is the RF flip angle.

Having calculated the AIF and the tissue CA concentrations, the obtained concentration time courses can be fitted to an appropriate PK model.

# Chapter 5

## Materials and methods

### 5.1 DCE-MRI renography

When the contrast agent is injected into the bloodstream, it starts its journey via the organism. It travels through the abdominal aorta, which branches into the left and right renal arteries supplying the kidneys with the blood.

First, the CA reaches the renal cortex, where a portion of it is filtered by the glomerulus from the blood to the Bowman's capsule in the process of glomerular filtration. Next, it is passed by the renal tubule to the renal medulla to finally be collected by the collecting system. Chemicals such as gadolinium-based markers used in DCE-MRI that are freely filtered but neither reabsorbed nor secreted by the kidneys can be used for estimating the glomerular filtration rate in quantitative DCE-MRI analysis.

This part of the thesis describes in details the implemented method of the quantitative analysis of the kidney's function from DCE-MRI. The chapter leads the reader through the subsequent steps of image processing and analysis to finally compare the performance of the chosen PK models. The aim is to choose the model,

which allows for obtaining the best results for GFR estimation on the given data and to draw a conclusion if it can be considered a robust, reliable method for the future applications.

## 5.2 DCE-MRI acquisition

The dataset used in this project consists of forty DCE-MRI sequences. Each of the twenty healthy, non-smoking participants underwent two MRI examinations at a time interval of 7 days. Gd-DOTA (*gadoteric acid*), which is a gadolinium-based CA, at a dose of 0.025 mmol/kg was administrated as a bolus injection at 3 mL/s in an antecubital vein followed by a 20 mL saline flush. The examinations were performed on the 32 channel 1.5 T whole-body scanner (Siemens Magnetom Avanto [46]) with a gradient strength = 45 mT/m and slew rate = 200 mT/m/ms using a standard six-channel body matrix coil and table-mounted six-channel spine matrix coil for signal reception. The 74 volumes, each consisting of 30 slices, covering the kidneys and the aorta were continuously acquired every 2.3 s for approximately 6 min in coronal-oblique plane. The acquisition matrix was  $192 \times 192$  whereas the voxel size was equal to  $2.2 \times 2.2 \times 3$  mm<sup>3</sup>. The parameters of the used spoiled gradient recalled 3D FLASH pulse-sequence were: echo time,  $TE = 0.8$  ms, repetition time,  $TR = 2.36$  ms, flip angle,  $\alpha = 20^\circ$ .

More information about the acquisition of DCE-MRI data used in this project can be found in [47]. A few frames of the sample raw DCE-MRI sequence are shown in Figure 5.1.

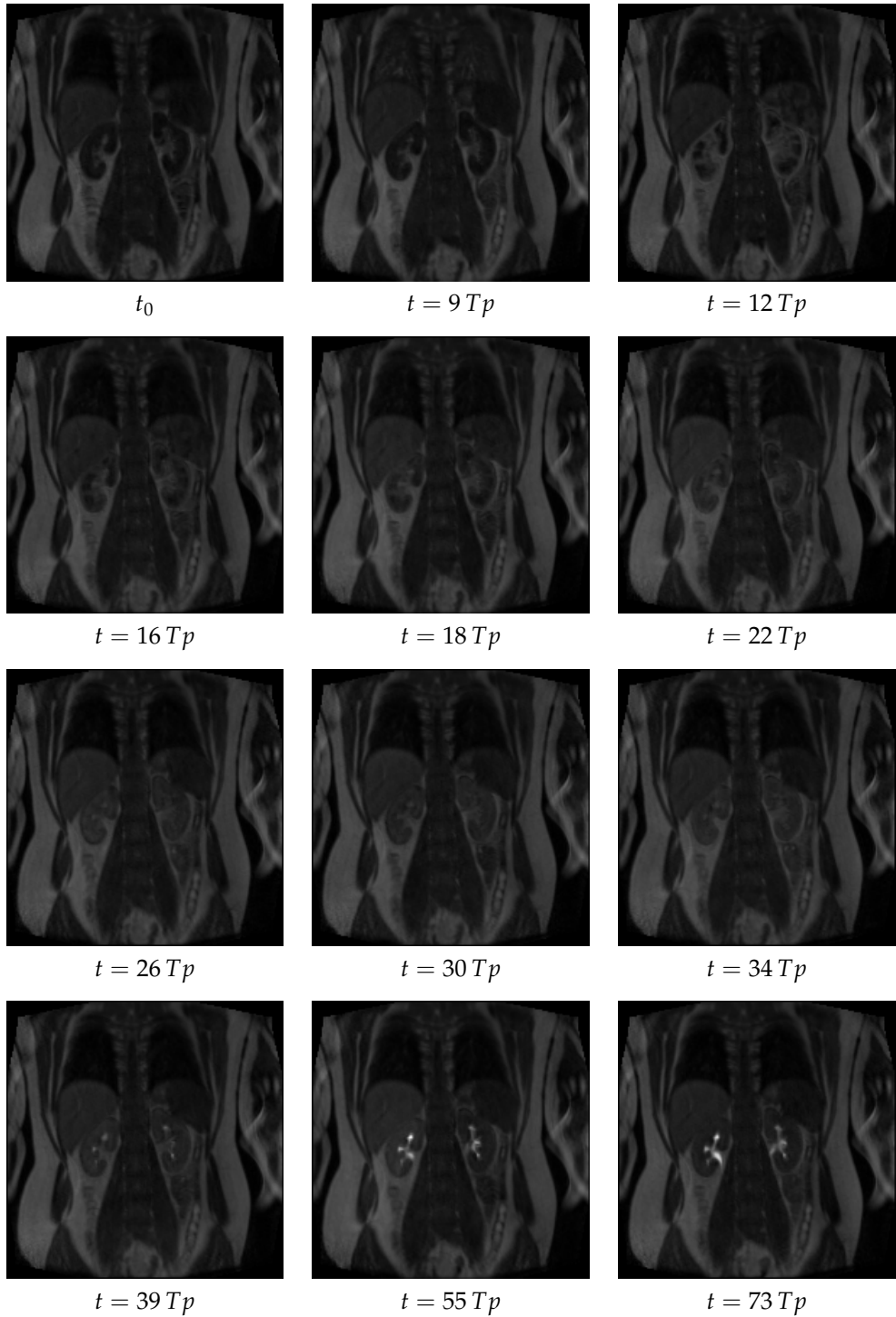


**Figure 5.1.** Sample DCE-MRI sequence of the healthy kidneys.  $Tp$  is a given time point. Firstly, the signal enhancement is observed in the renal cortex. Then, the tracer travels to the renal medulla and finally is collected by the collecting system.

## 5.3 GFR reference values

Next to the DCE-MRI examinations, the participants had their GFR assessed by two chemical methods commonly used in the clinical practice: the *serum-creatinine* (SCr) blood test and *iohexol-GFR* tests. Creatinine is an endogenous indicator, which allows for estimating GFR from validated algorithms. Iohexol in terms is an exogenous marker which is used for accurate GFR measurement. The clinical characteristics of all the participants are included in Table 5.1

**Table 5.1.** Clinical characteristics of the participants [47].

Participants	20
Gender (female/male)	16/4
Age (years)	25 (20–38)
Height [m]	1.71 ± 0.07
Weight [kg]	66.2 ± 8.7
Body Mass Index (BMI) [kg/m <sup>2</sup> ]	22.6 ± 2.1
Body Surface Area (BSA) [m <sup>2</sup> ]	1.77 ± 0.14 (1.5–2.0)
Iohexol GFR [mL/min/m <sup>2</sup> ]	103 ± 10 (87–125)
SCr GFR [mL/min/m <sup>2</sup> ]	110 ± 15 (81–128)

Values in parentheses are ranges.

Plus minus values are means ± standard deviations (SD).

## 5.4 Image processing and analysis

### 5.4.1 Motion correction

One of the first fundamental problem encountered during DCE-MRI analysis is misalignment of the 3D volumes across time slices. This misalignment of organs is a result of the patient's respiratory motion as well as the heartbeat and bowel peristalsis and is unavoidable during examination. Studies have shown that even

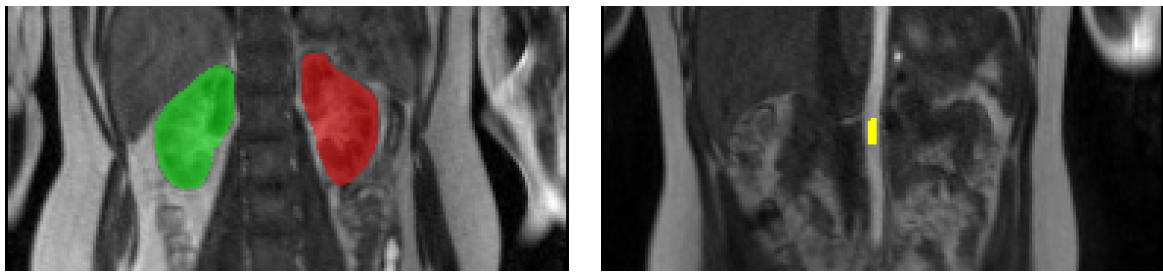
slight misalignment can lead to significant differences in intensity time courses [48] and thus, motion correction of time series is essential for further analysis.

In order to remove the motion artifact, all files were motion-corrected across time points. For this purpose the R programming language for statistical computing and graphics was used [49] together with the package ANTsR [50], which provides quantification tools for biomedical images.

As an initial step, for every time series, the algorithm extracts the 3D volumes. Each extracted volume corresponds to the data obtained in one time point. Next, the average image of the temporal volumes is calculated, which serves as a target image for image registration. Every temporal volume is then aligned to it and at the end they are combined back together into the 4D time series. As the misalignment concerns the inner structures, not the whole body and various organs have spatially variant geometric differences, the modality of choice was the *symmetric normalisation* (SyN) algorithm, which is the non-rigid deformable transformation utilizing *cross-correlation* (CC) as a similarity metric [51–53].

#### 5.4.2 Manual labelling

In the next step, the labels of the whole left and right kidney were created. For this purpose the 3D volumes were extracted for each time frame and the slice with maximal signal enhancement of the kidneys was chosen (usually between 12–17 time slice). In this image, left and right kidney were manually delineated in coronal plane using the ITK-Snap software [54]. Additionally, a few voxels of aorta (15–20) were labelled on maximal aortic enhancement time slice (9–10). So obtained labels were then combined and propagated across the time points. The sample labels are shown in Figure 5.2. All further analysis was implemented in the Python programming language v. 3.6 [55].



(a) Labels of the left and right kidneys.

(b) Label of the aorta.

**Figure 5.2.** Sample labels of kidneys and aorta. Green and red are labels of the right and left kidney respectively, whereas yellow is the aorta label.

### 5.4.3 Pelvis region removal

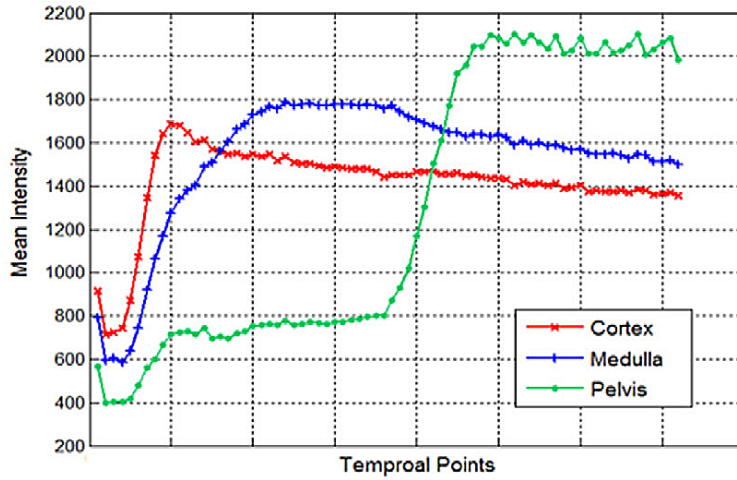
Due to the fact that glomerular filtration takes place in renal parenchyma, the region of pelvis had to be removed from further analysis.

Resulting from the physiology of the process, the three renal compartments (cortex, medulla, pelvis) can be distinguished from each other on the basis of their time courses, as shown in Figure 5.3. Depending on the compartment, the rapid enhancement of the signal occurs in different periods, which makes the shapes of the time intensity curves very unique. From the Figure 5.3 it can be seen that the highest variation is observed between pelvis and two other renal compartments. Consequently, it can be separated by unsupervised clustering.

First of all, each voxel included in the label of the kidney was described by the vector of seventy-four features as follows:

$$\mathbf{v}_{ijk} = [S(0), S(1), \dots, S(72), S(73)], \quad (5.1)$$

where  $S(n)$  is the value of signal intensity at the time point  $n$ .

**Figure 5.3.** Example kidney compartments time courses [48].

However, feature space of seventy-four dimensions is way too large for further analysis. High dimensionality of raw DCE-MRI data results in computational complexity, and thus memory and time consumption as well as numerical problems. What is more, it contains a lot of noise [48]. To overcome this problems, the *principal component analysis* (PCA) [56] was applied.

PCA is a statistical procedure, which transforms the number of interrelated features into smaller set of uncorrelated variables. These so-called *principal components* (PCs) are the linear combinations of the original variables [57]. As a result, after rotating the feature space, the first PC contains most variance, the last one the least and so on. In this way the dominant patterns are extracted, while the noise is reduced [56, 58]. Further, every of the PC is characterised by a ratio of *explained variance*, which indicates the portion of the dataset's variance lying along the axis of each PC [59].

Applying the theory to practice, each voxel belonging to the kidney, initially described by the seventy-four features was described by a number of PCs:

$$\mathbf{v}_{ijk} = [PC1, PC2, \dots, PCn] \quad (5.2)$$

The amount of PCs,  $n$ , was chosen as a minimum number of dimensions required to preserve 95% of the data's total variance so that the sum of the explained variances of  $n$  PCs was equal to at least 0.95 (usually between 4–6 PCs). The visual representation of the feature space with first three dimensions (PCs) for sample kidney is shown in Figure 5.4. Note that for better understanding, the clusters were already marked with different colors.

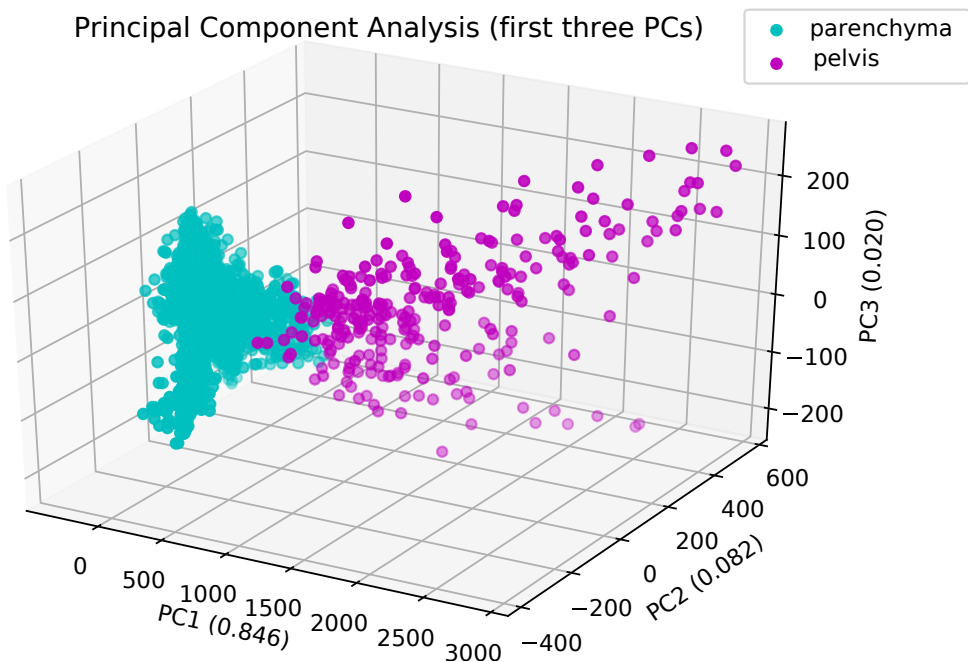


**Figure 5.4.** Principal component analysis for a sample kidney. The values in brackets are the ratios of explained variance for the given PCs. Note that the number of PCs was reduced to three for visualisation purpose.

To the dimensionally reduced data, the *k-means clustering* was applied in order to separate voxels into two groups: pelvis and renal parenchyma. The k-means is an unsupervised clustering algorithm aiming to divide the data into groups so that the diversity between the groups and the similarity within the single group are maximised [60].

Given a data set  $X = \{\vec{x}_1 \dots \vec{x}_n\}$  in  $m$ -dimensional space (which actually corresponds to the  $m$  features of a sample) the algorithm's objective is to minimize the square error function given by [60, 61]:

$$J = \sum_{j=1}^k \sum_{x_i \in S_j} (||x_i - c_j||)^2, \quad (5.3)$$

where  $||x_i - c_j||$  is the Euclidean distance between a data point  $x_i$  and the cluster centre  $c_j$  of cluster  $S_j$  from  $k$  predefined clusters. It is achieved in the steps summarised in Algorithm 1.

---

**Algorithm 1. K-means clustering**


---

**Input** : number of clusters  $k$ ,

set of points in  $m$ -dimensional space:  $X = \{\vec{x}_1 \dots \vec{x}_n\}$

**Output:** set of cluster labels of  $X$ :  $L = \{l(\vec{x}_i) | i \in \{1 \dots n\}\}$ ,

coordinates of cluster centroids:  $(\vec{c}_1 \dots \vec{c}_k)$

```

1  $(\vec{c}_1 \dots \vec{c}_k) \leftarrow \text{RandomlyChooseCentroids}(k, X)$   $(\vec{c}_1 \dots \vec{c}_k) \in X$ 
2 repeat
3   /* assign each data point to the closest centroid on the basis of
    Euclidean distance */  

4    $l(\vec{x}_i) \leftarrow \text{argminDistance}(\vec{x}_i, \vec{c}_j) | j \in \{1 \dots k\}$ 
5    $(\vec{c}_1 \dots \vec{c}_k) \leftarrow \text{CalculateMeanOfPointsInCluster}()$       /* recalculate centroids */
6 until none of  $(\vec{c}_1 \dots \vec{c}_k)$  changes
7 return  $L, (\vec{c}_1 \dots \vec{c}_k)$                                      /* points divided into clusters */

```

---

To segment the kidney, the k-means algorithm was initiated with two clusters,  $k = 2$  and performed for points (kidney voxels) in  $m$ -dimensional space ( $m$  is the number of PCs). Further, for each of the identified clusters, the average time point,  $T_{max}$  in which signal intensity reaches its maximum was calculated. Following the assumption that  $T_{max\_pelvis} > T_{max\_parenchyma}$ , the cluster with greater  $T_{max}$  was marked as the pelvis and removed from the ROI. The average time-intensity curves

for two detected clusters in k-means clustering algorithm for sample kidney are presented in Figure 5.5. One can easily note that the wash-in phase in pelvis takes place much later than in renal parenchyma. The results of the segmentation in turn are shown in Figure 5.6.

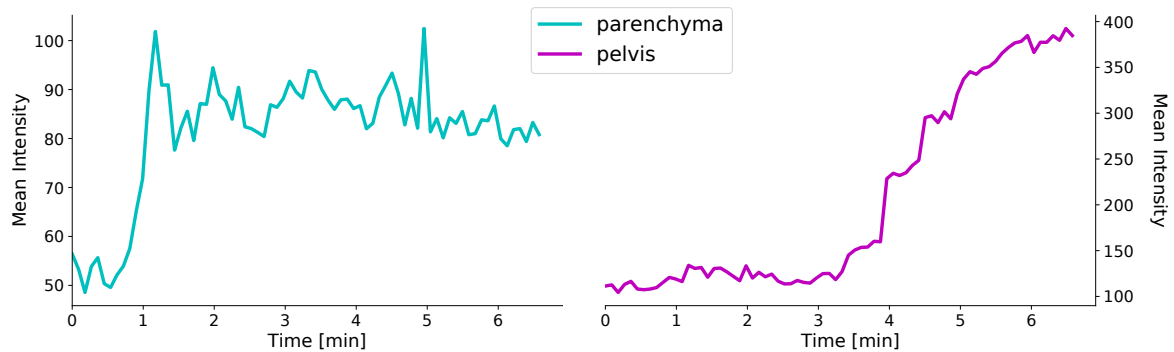


**Figure 5.5.** Average time courses for two clusters detected in k-means algorithm performed for sample kidney.

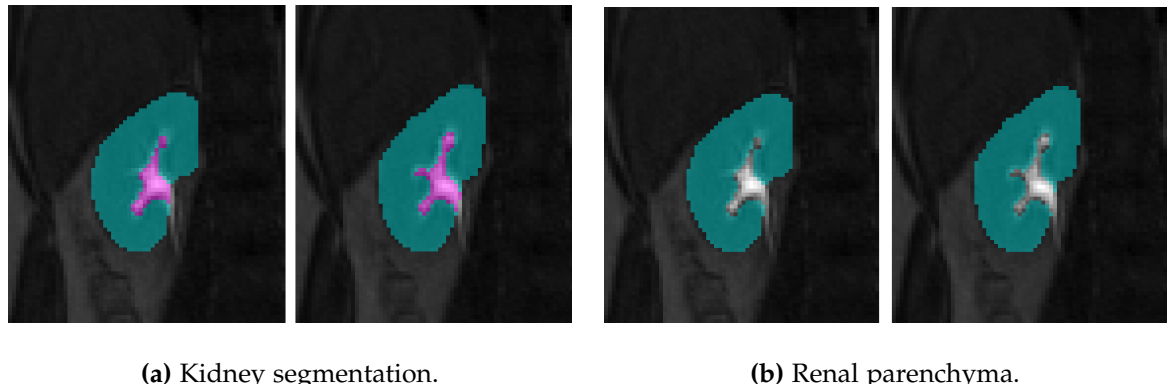


**Figure 5.6.** The results of the segmentation obtained with k-means clustering. Figure (a) shows two regions of a sample kidney: the pelvis (magenta) and the renal parenchyma (cyan); Figure (b) presents the kidney after pelvis removal. The images were intentionally presented at Time point  $t = 73 T_p$ , when the enhancement of the pelvis is high, for better visualisation.

#### 5.4.4 Concentration-time curves

Having labelled the proper ROI, the time has come for the principal part of the analysis, namely pharmacokinetic modelling. The whole PK part was implemented in the Python programming language from the scratch and no ready toolboxes for PK modelling were used.

All PK models used during quantitative DCE-MRI analysis call for determining both the tissue,  $C_t(t)$ , and blood plasma,  $C_p(t)$ , concentration as a function of time. In our case, the  $C_t(t)$  is the mean concentration in renal parenchyma, whereas the  $C_p(t)$ , can be derived from the AIF, which is a concentration in a blood vessel feeding the kidney (aorta). Thus, they were calculated in the next steps of the project.

For each of the kidney, as well as for the aorta, the mean intensities of the voxels included in the particular labels were calculated at the each time point and the intensity time courses were plotted. Sample time courses are shown in Figure 5.7.

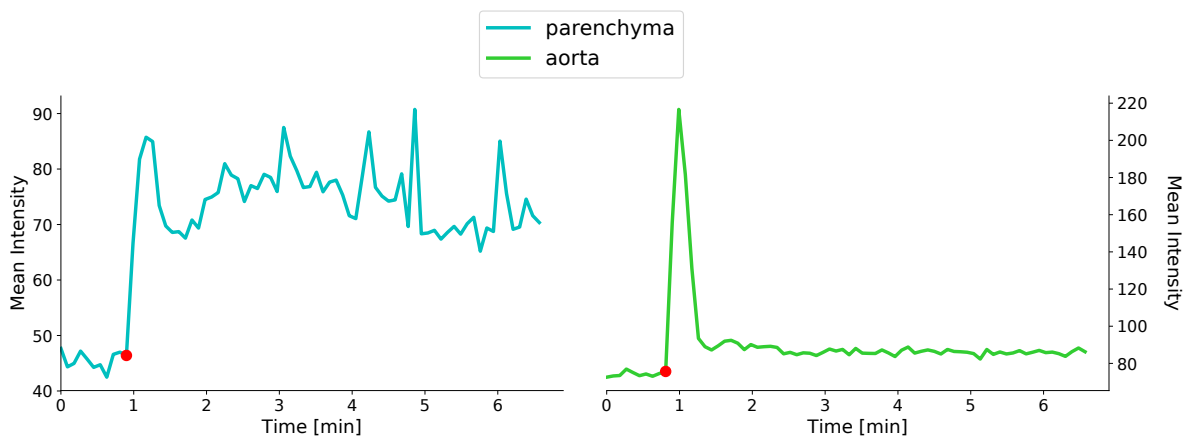


**Figure 5.7.** Sample average time-intensity curves for a kidney and aorta. Red dot is  $T_{baseline}$ , the last point of the baseline.

Assuming the linear relation between tracer concentration and signal intensity  $S(t)$  dictated by the low dose of Ga-based CA, the tracer concentration can be expressed as:

$$C(t) = S(t) - S_0, \quad (5.4)$$

where  $S_0$  is the baseline signal, which is the average signal intensity among the time before the administration of CA. In order to determine  $S_0$ , the time point before rapid signal increase,  $T_{baseline}$  had to be found as marked with red dot in Figure 5.7.

To achieve it, firstly, for the purposes of the examination of the function changes, the median filter with the *kernel size* = 5 was applied in order to smooth the signal and eliminate artificial peaks and valleys, as shown in Figure 5.8. In next step, for every intensity time course under analysis, its derivative was calculated. The derivative describes the instantaneous rate of change of the function. It tells how fast the output of the function (signal intensity) changes compared to the independent variable (time) [62] and seems to be a perfect solution to the problem, which boils down to finding the most rapid signal change. Because of one's interests is detection only of the function's increases, not decreases, the points, in which the derivative is negative were neglected,  $S'(t) < 0 \leftarrow 0$ . So modified derivative of the sample kidney and aorta are shown in Figure 5.9.

Now, all that had to be done to find  $T_{baseline}$  was to detect the point, in which the derivative of the signal intensity time course reaches its maximum,  $T_{baseline} = argmax S'(t)$ . Having it determined, the  $S_0$  was calculated as the mean signal intensity value from the beginning of the measurement ( $t = 0$ ) to  $T_{baseline}$ . Finally, the CA concentration in the tissue and aorta were calculated according to Formula (5.4). The results of intensity-concentration conversion for sample time curves are shown in Figure 5.10.

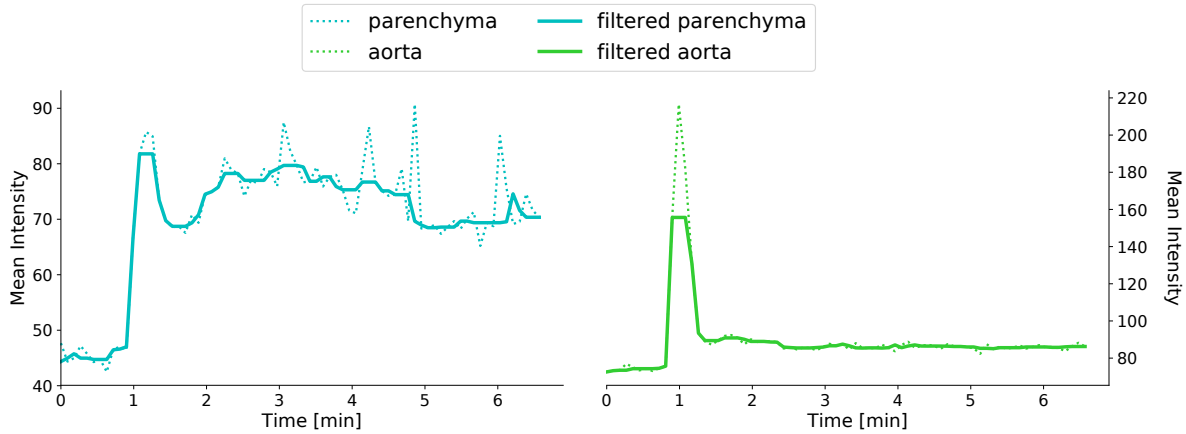


**Figure 5.8.** Sample average time-intensity curves for a kidney and aorta with applied median filter. Note that cut peak of the aorta's signal is a result of the median filter and it is present only during the baseline removal step.

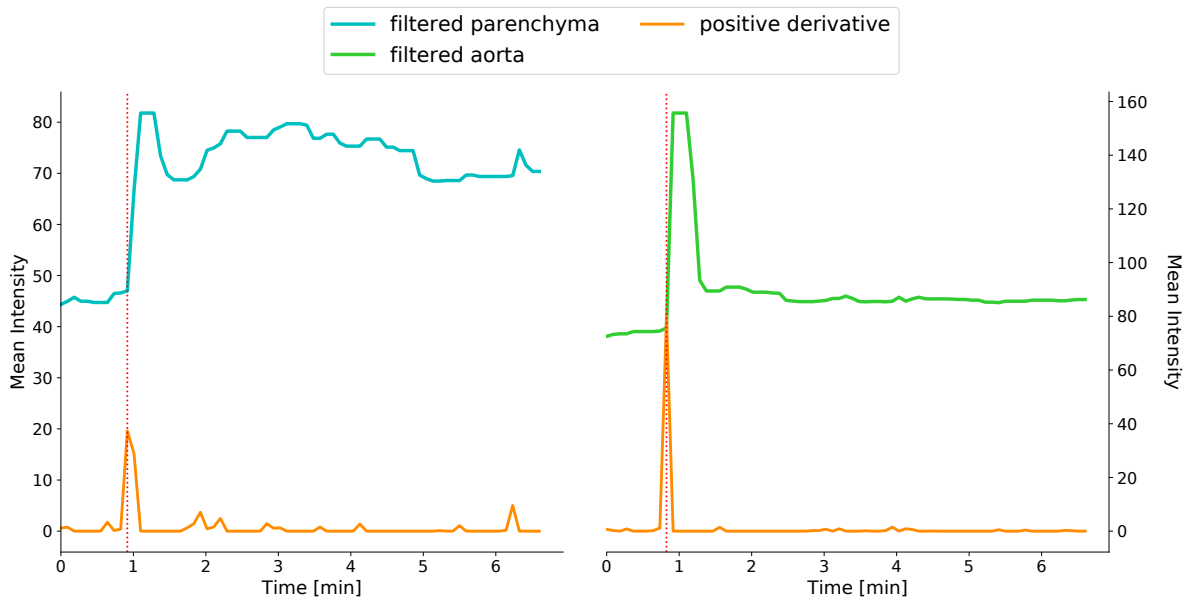


**Figure 5.9.** Positive derivative of a sample kidney and aorta intensity time courses. The vertical line indicates the time point, in which the derivative reaches its maximal value.

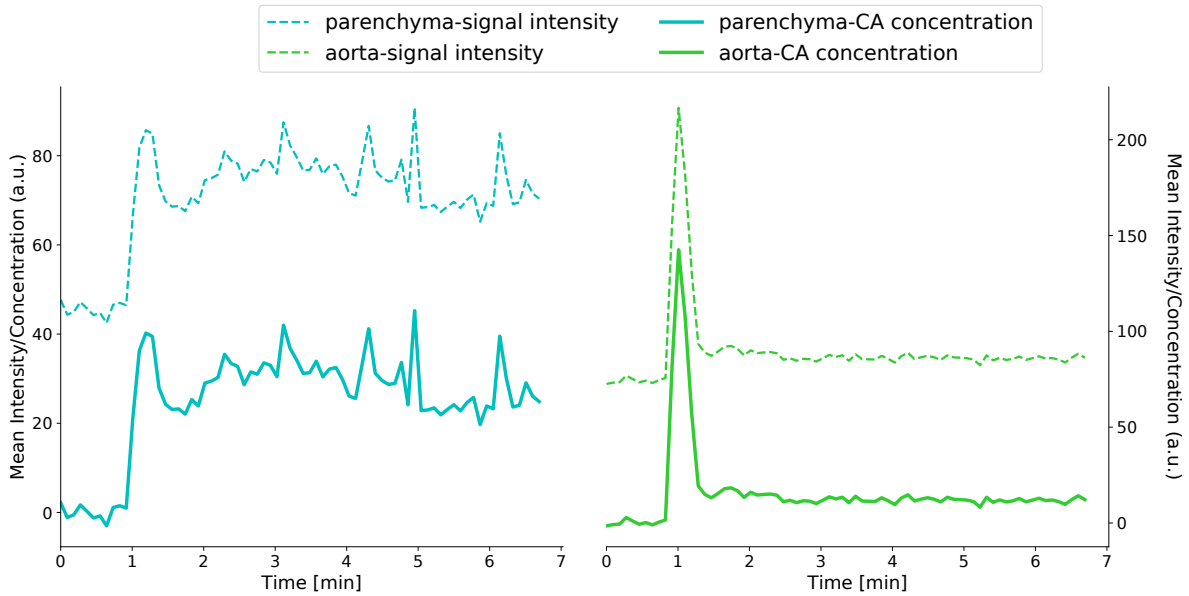


**Figure 5.10.** Time-intensity curves of a sample kidney and aorta converted into the concentration-time curves.

#### 5.4.5 Pharmacokinetic modelling

Having determined the AIF and the concentration time course for the renal parenchyma, almost all components necessary for the renal quantitative evaluation were obtained. Almost, but not all. One should take into consideration the fact that AIF is the concentration of CA in the blood of the aorta, which consist of both the red blood cells and the blood plasma. Gadolinium-based contrast agents, however, distribute in plasma rather than whole blood, so their effective plasma concentrations must be considered. Thus, the *hematocrit* (Hct) correction was performed as follows [63]:

$$C_p(t) = \frac{C_a(t)}{1 - Hct}, \quad (5.5)$$

where  $C_p$  is CA plasma concentration,  $C_a$  is concentration in the aorta defined by the AIF and  $Hct$  is the fractional volume of red blood cells in the blood. In this study, its value was taken from the literature as an average population value and

was equal to  $Hct = 0.42$  [63].

Finally, PK modelling could have been performed. The models of choice were the Tofts and Kermode model, extended Tofts and Kermode model, Patlak-Rutland model and two-compartment exchange model. The aim was to obtain value of the transfer constant  $K_{trans}$  [ $\text{min}^{-1}$ ], which corresponds to the GFR per unit tissue volume. The fit was performed by using a non-linear least squares analysis.

**Tofts and Kermode model.** According to the *Tofts and Kermode* (TK) model [43] the tracer is distributed in two compartments: intravascular and *extravascular extracellular space* (EES). The tracer diffuses from the blood plasma at rate specified by the transfer constant  $K_{trans}$  [ $\text{min}^{-1}$ ] and returns at the reverse transfer rate  $k_{ep} = K_{trans}/v_e$  [ $\text{min}^{-1}$ ]. This model assumes, however, that the amount of intravascular (plasma) tracer is negligible comparing to the tissue signal. The tissue concentration,  $C_t(t)$ , is then given by [9]:

$$C_t(t) = v_e C_e(t), \quad (5.6)$$

where  $v_e$  is EES fractional volume and  $C_e(t)$  is EES concentration. The system can be described by mass balance equation [9, 64]:

$$\frac{dC_t(t)}{dt} = K_{trans}(C_p(t) - C_t(t)/v_e), \quad (5.7)$$

where and  $C_p(t)$  is blood plasma concentration, The solution obtained according to the procedure presented in Chapter 4 is [9, 42]:

$$C_t(t) = C_p \circledast K_{trans} e^{-k_{ep}t} = K_{trans} \int_0^t C_p(\tau) e^{-k_{ep}(t-\tau)} d\tau \quad (5.8)$$

**Extended Tofts and Kermode model.** While the Tofts model neglects intravascular contribution assuming weak vascularization of the tissue, the *extended Tofts and Kermode* (ETK) model [44] does take it into account. According to ETK, the tissue concentration is described by the formula [9, 63]:

$$C_t(t) = v_p C_p(t) + v_e C_e(t), \quad (5.9)$$

where  $v_p$  is fractional plasma volume. The differential equation describing the EES compartment is [42]:

$$v_e \frac{dC_e(t)}{dt} = K_{trans}(C_p(t) - C_e(t)) \quad (5.10)$$

Solving the equation and substituting to (5.9) the tissue concentration boils down to [9, 63]:

$$\begin{aligned} C_t(t) &= v_p C_p(t) + C_p \circledast K_{trans} e^{-k_{ep}t} = \\ &= v_p C_p(t) + K_{trans} \int_0^t C_p(\tau) e^{-k_{ep}(t-\tau)} d\tau \end{aligned} \quad (5.11)$$

In TK and ETK models the free parameters  $K_{trans}$ ,  $v_e$  and  $v_p$  are estimated by fitting the model to obtained in DCE-MRI examinations time-concentration curves.

**Patlak-Rutland model.** Unlike the TK and ETK models, the *Patlak-Rutland* model [45] assumes that reverse transfer constant from the EES to the plasma,  $k_{ep}$ , is negligibly small, because of the short time of the measurement (tracer does not have time to return) and low permeability [9]. Similarly to the ETK, the tissue concentration is equal to:

$$C_t(t) = v_p C_p(t) + v_e C_e(t) \quad (5.12)$$

However, the tracer change in EES is equal to [41, 45]:

$$v_e \frac{dC_e(t)}{dt} = K_{trans} C_p(t) \quad (5.13)$$

Solving the Equation (5.13) and substituting into Formula (5.13) [9, 45]:

$$C_t(t) = v_p C_p(t) + K_{trans} \int_0^t C_p(\tau) d\tau \quad (5.14)$$

To obtain the free parameters, the concentration time courses obtained from DCE-MRI examination can be fitted directly to Formula (5.14) or the graphical approach called the *Patlak plot* can be applied. In this approach the above equation is linearised as [9, 45]:

$$Y = K_{trans} X + v_p, \quad (5.15)$$

where  $Y = C_t(t)/C_p(t)$  and  $X = \int_0^t C_p(\tau) d\tau/C_p(t)$ . The free parameters  $K_{trans}$  and  $v_p$  can be then estimating by constructing a linear plot and calculating its slope and intercept respectively. In this project, the data was fitted to Formula (5.14).

**Two-compartment exchange model.** While all the previously described models allow for estimating transfer constant  $K_{trans}$  combining both the plasma blood flow, and the tissue permeability, *two-compartment exchange model* (2CXM) enables their separate estimation. According to 2CXM, the plasma compartment has an arterial inlet and a venous outlet of the same plasma flow,  $F_p$  [ $\text{min}^{-1}$ ]. The tracer is exchanged between the two compartments: EES and intravascular plasma, at a symmetric rate quantified by the permeability surface product,  $PS$  [ $\text{min}^{-1}$ ]. Because the CA leaves the system, the model is referred to as an open system. Similarly to PR and ETK models the tissue concentration is expressed as [9]:

$$C_t(t) = v_p C_p(t) + v_e C_e(t) \quad (5.16)$$

The system is described by a pair of mass balance differential equations [9]:

$$v_p \frac{dC_p(t)}{dt} = F_p(C_a(t) - C_p(t)) + PS(C_e(t) - C_p(t)) \quad (5.17)$$

$$v_e \frac{dC_e(t)}{dt} = PS(C_p(t) - C_e(t)) \quad (5.18)$$

Note that in 2CXM the CA concentration in the plasma of the feeding artery is denoted as  $C_a$  ( $C_p$  in previous models) whereas  $C_p$  is CA concentration in intravascular plasma. The solution boils down to [9]:

$$\begin{aligned} C_t(t) &= F_p(Be^{-m_1 t} + (1-B)e^{-m_2 t}) \circledast C_a = \\ &= F_p \int_0^t (Be^{-m_1 \tau} + (1-B)e^{-m_2 \tau}) C_a(t-\tau) d\tau, \end{aligned} \quad (5.19)$$

where  $m_1$ ,  $m_2$  and  $B$  are defined as:

$$m_1 = \frac{1}{2} \left( a + b + \sqrt{(a+b)^2 - 4bc} \right) \quad (5.20)$$

$$m_2 = \frac{1}{2} \left( a + b - \sqrt{(a+b)^2 - 4bc} \right)$$

$$B = \frac{m_2 - c}{m_2 - m_1},$$

where

$$a = \frac{F_p + PS}{v_p}, \quad b = \frac{PS}{v_e}, \quad c = \frac{F_p}{v_p} \quad (5.21)$$

The  $K_{trans}$  can be then obtained by:

$$K_{trans} = \frac{PS \cdot F_p}{PS + F_p} \quad (5.22)$$

A sample concentration time course fitted to different models is shown in Figure 5.11.

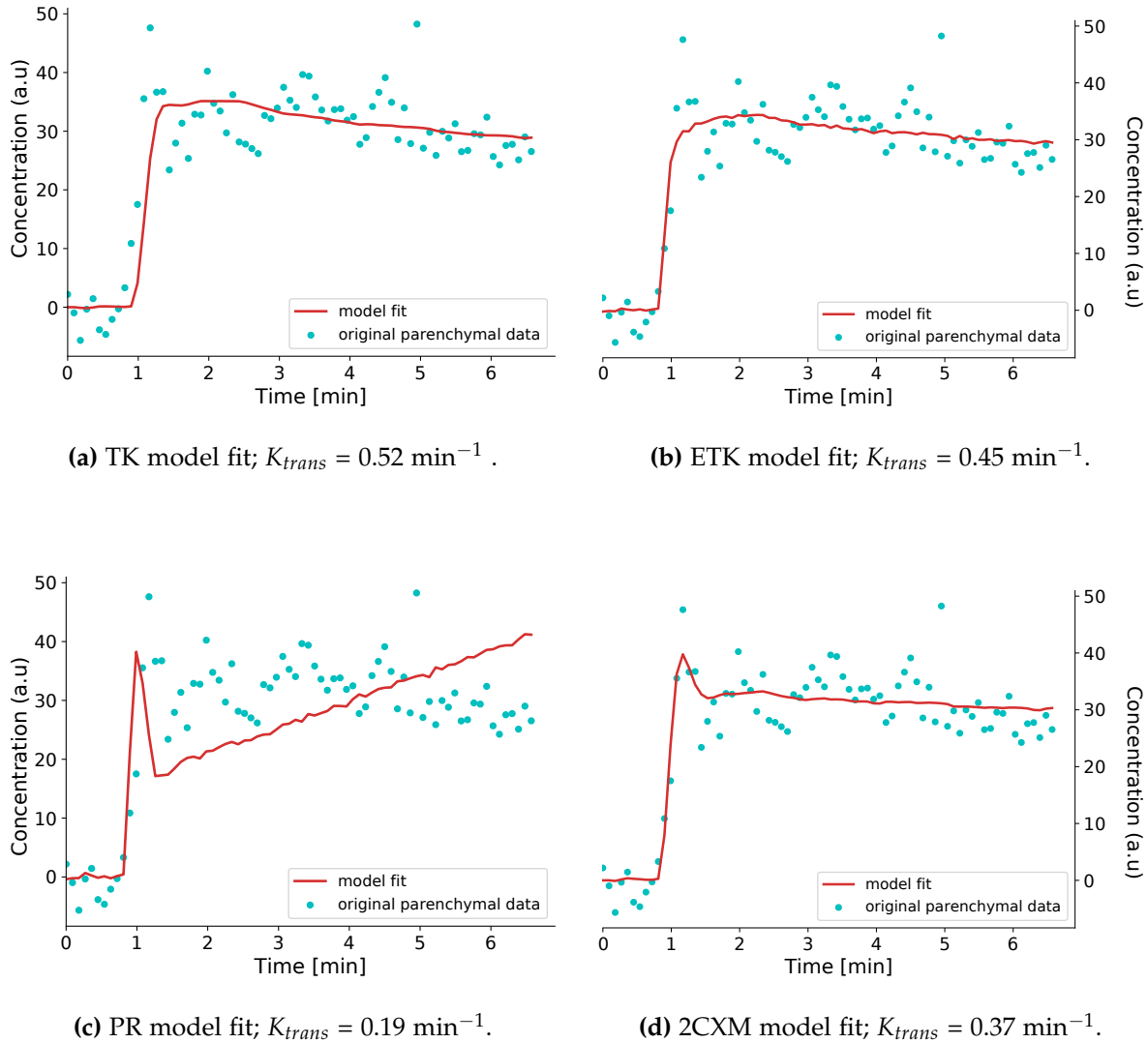


**Figure 5.11.** A sample concentration time course fitted to different PK models: (a) Tofts and Kermode model (b) extended Tofts and Kermode model (c) Patlak-Rutland model (d) two-compartment exchange model.

#### 5.4.6 GFR estimation

Having estimated the transfer constant  $K_{trans}$  the *Single Kidney GFR* (SKGFR) could have been calculated according to the formula:

$$SKGFR = K_{trans} V_{parenchyma}, \quad (5.23)$$

where  $V_{parenchyma}$  is the parenchymal volume (in mL) of the examined kidney given by:

$$V_{parenchyma} = n V_{voxel}, \quad (5.24)$$

where  $n$  is the number of voxels included in the kidney label whereas  $V_{voxel}$  is the volume of the voxel ( $2.2 \times 2.2 \times 3 \text{ mm}^3 = 0.14252 \text{ mL}$ ). Total GFR for each dataset was then calculated by summing up the SKGFR of the left and right kidneys. All obtained GFR values were normalised for standard BSA ( $1.73 \text{ m}^2$ ).

# Chapter 6

## Results

The algorithm developed within this thesis was evaluated on ten DCE-MRI sequences of ten different participants. For each of the participant one of the two DCE-MRI sequences was chosen randomly.

The segmentation of the pelvis was evaluated with *Dice similarity coefficient* (DC) given by the formula [65]:

$$DC = \frac{2|A \cap B|}{|A| + |B|}, \quad (6.1)$$

where  $|A|$  and  $|B|$  are the number of voxels in pelvis detected in the automatic segmentation routine and the number of voxels in ground truth labelled organoleptically, respectively, whereas  $|A \cap B|$  is the number of common voxels. The average accuracy of the pelvis segmentation was equal to  $DC = 0.86 \pm 0.06$ .

The SKGFR values of the left and right kidney, as well as total GFR for each of the participants obtained in the examination of the MRI sequences applying different PK models are shown in Table 6.1. Also, the GFR values obtained with chemical methods were included in the table for comparison. *Measured GFR* (mGFR) is a value obtained in iohexol-GFR test, whereas *estimated GFR* (eGFR) is the one derived from the SCr blood test.

For each of the method (different PK models and SCr blood test) its degree of agreement with the reference method (iohexol-GFR test) was assessed. For this purpose the Bland–Altman plots [66] were drawn as shown in Figure 6.1. This type of plot is a scatter one, in which the difference between the measurement of the examined method and the reference method is plotted against the average of these measurements. The plot indicates the central tendency (bias) as the robust grey line calculated as the mean difference of the measurements. The so-called *limits of agreement* (LoA) are denoted as grey dashed lines and indicate the interval, within which 95% of the measurements is expected to lay.

**Table 6.1.** GFR values derived from DCE-MRI using different PK models and values obtained with chemical methods.

No.	mGFR	eGFR	MRI GFR											
			TK			ETK			PR			2CXM		
			L	R	T	L	R	T	L	R	T	L	R	T
1	97	126	85	82	167	66	61	127	25	23	48	42	31	72
2	100	111	75	62	137	61	53	115	21	20	41	61	50	111
3	104	125	48	62	111	42	53	95	18	22	40	39	44	83
4	101	116	55	49	105	47	42	89	14	12	26	61	53	114
5	90	80	71	76	146	61	62	123	17	17	34	38	34	72
6	89	93	42	48	90	34	40	74	12	15	27	42	37	79
7	102	114	48	52	100	36	39	75	11	13	25	51	51	101
8	103	123	50	61	111	38	47	85	12	13	25	48	51	99
9	87	100	44	64	108	35	57	92	18	25	42	52	37	89
10	97	115	59	64	123	46	50	96	17	18	35	52	47	100

L and R are SKGFR for left and right kidneys, respectively, whereas T is the total GFR.

TK, ETK, PR, 2CXM are particular PK models.

Note that  $L + R = T$  is not always satisfied because of the rounding error.

All GFR values are expressed in  $\text{mL}/\text{min}^{-1}/1.73 \text{ m}^2$ .

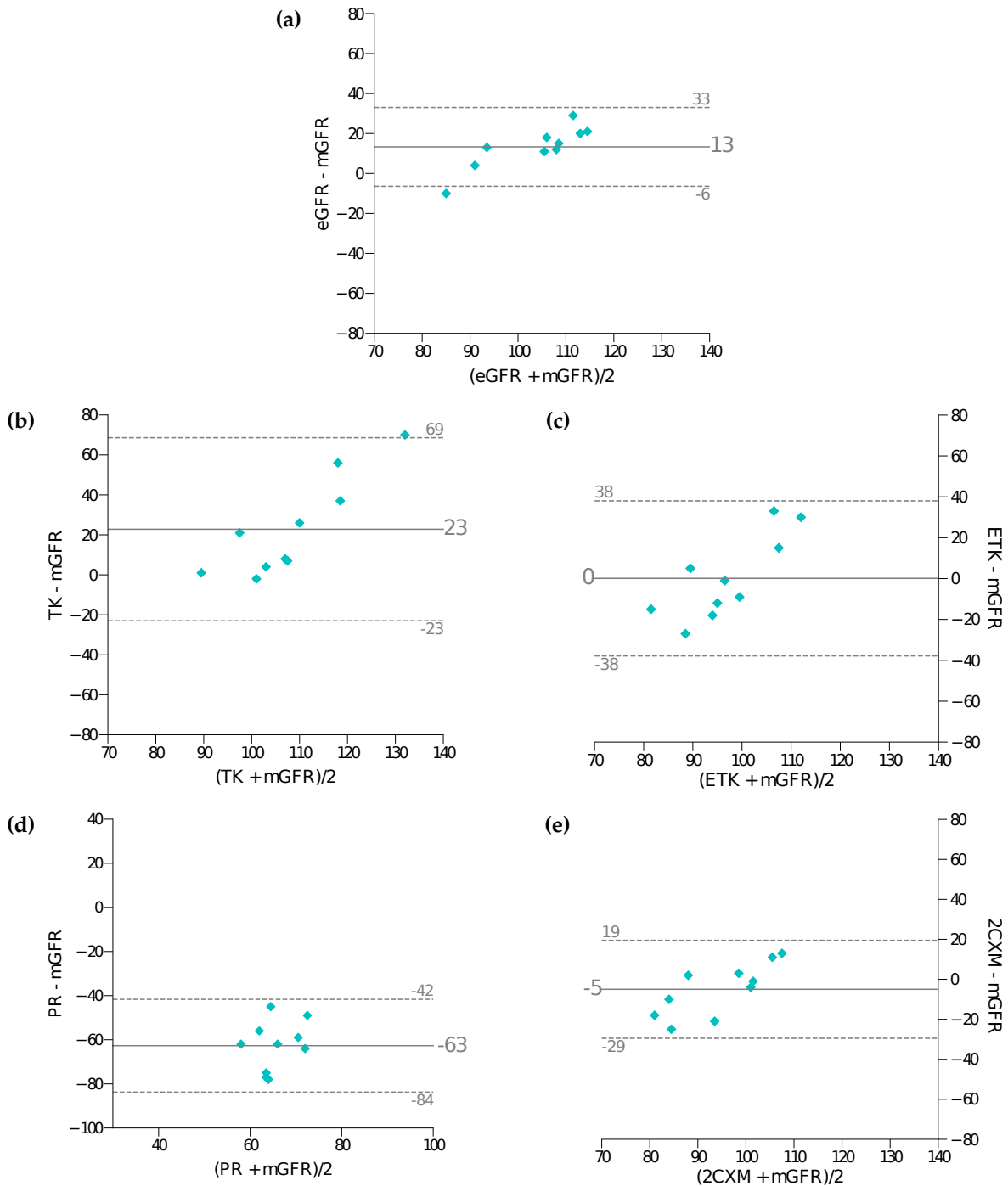


**Figure 6.1.** Bland–Altman plots for eGFR and different PK models with mGFR as a reference. TK, ETK, PR, 2CXM are particular models. All measurements are given in mL/min/1.73 m<sup>2</sup>. Note that for PR model the scale is different because of large shifts.

Table 6.2 compares the performance of PK models and SCr blood test (eGFR). For every of the method the average absolute error, defined as the absolute difference between mGFR and GFR obtained by the particular method was calculated. The goodness of fit of the model was evaluated with *root mean squared error* (RMSE). Additionally, for every of the GFR measurement method, the P30 value was calculated, which is the percent of the measurements lying within  $\pm 30\%$  of the true value (iohexol-GFR).

**Table 6.2.** Average absolute error, root mean square error, P30, bias and limits of agreement for different GFR estimation methods.

Method	Average absolute error	RMSE	P30	bias	LoA
eGFR	15 $\pm$ 7	—	100 %	13	-6–33
TK	23 $\pm$ 24	6.91 $\pm$ 0.89	70 %	23	-23–69
ETK	16 $\pm$ 11	5.64 $\pm$ 0.63	80 %	0	-38–38
PR	63 $\pm$ 11	9.26 $\pm$ 1.27	0 %	-63	-84–-42
2CXM	11 $\pm$ 9	5.15 $\pm$ 0.60	100 %	-5	-29–19

Average absolute error, RMSE, bias and LoA are given in  $\text{mL}/\text{min}^{-1}/1.73\text{ m}^2$

Additionally, the correlations of the GFR values obtained by PK modelling and SCr test from mGFR were evaluated with the Pearson correlation coefficient,  $r$  and the p-value,  $p$  for this test was determined. Obtained values as well as the best linear fits are presented in Figure 6.2.

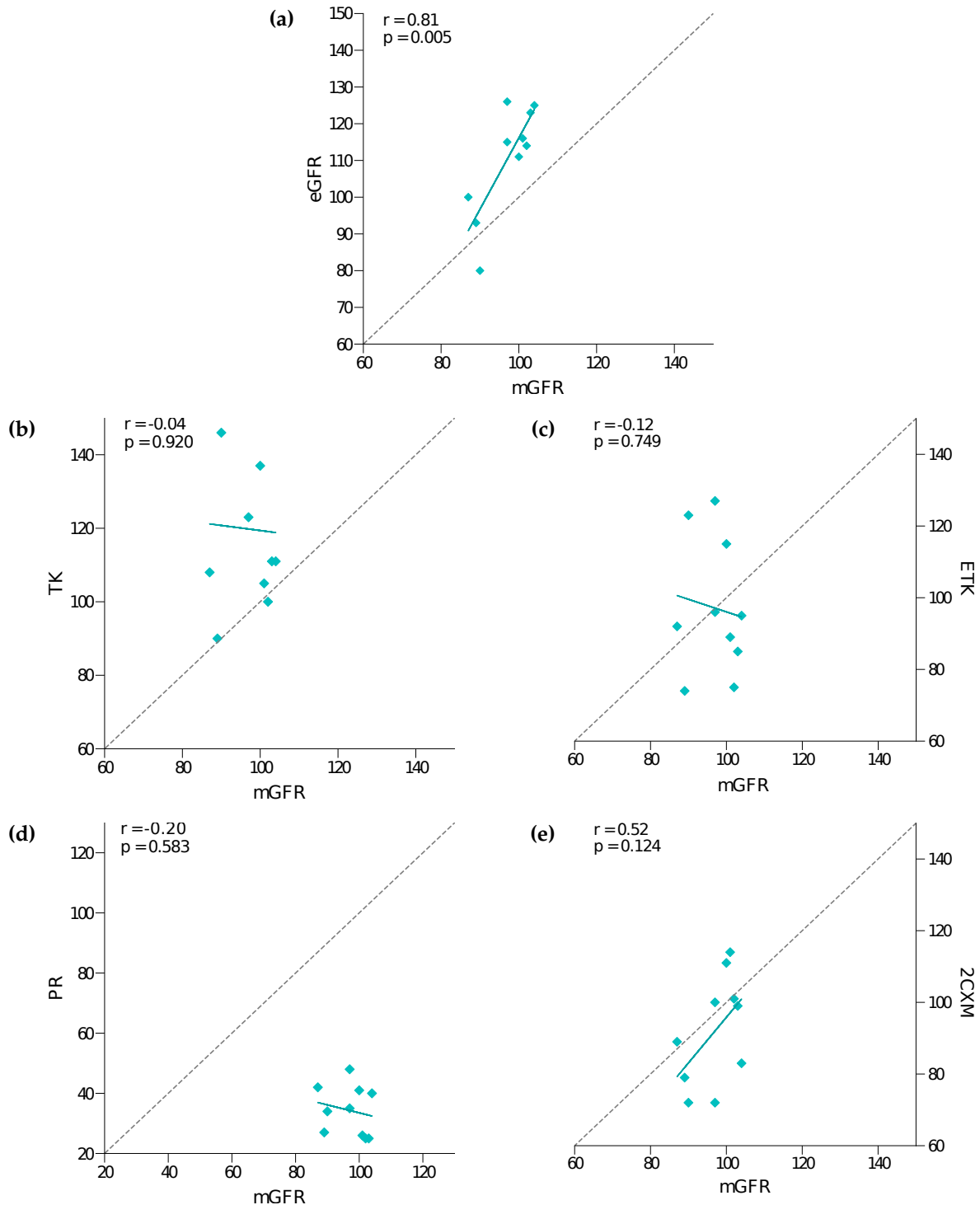


**Figure 6.2.** Relation between mGFR and (a) eGFR (b-e) different PK models. The dashed grey line indicates equality, whereas robust blue one the best linear fit. All measurements are given in mL/min/1.73 m<sup>2</sup>;  $r$ : Pearson correlation coefficient,  $p$  : p-value .

# Chapter 7

## Discussion

The aim of the study described in the previous chapter was to examine the performance of four pharmacokinetic models: TK, ETK, PR and 2CXM models.

The results showed that all PK models but the PR model give the realistic, normal GFR values, whereas the latter one underestimates it at least twice, and therefore it will be excluded from further discussion.

Regarding the accuracy, with reference to mGFR, the bias was equal to 13 for eGFR, 23 for TK model, 0 for ETK model, and -5 for 2CXM (all in mL/min/1.73 m<sup>2</sup>). What follows, TK and SCr test tend to slightly overestimate the true GFR. ETK and 2CXM models in terms showed to be the most accurate ones with bias equal or close to 0. What is more, the high accuracy of 2CXM and ETK was confirmed by the small average absolute error. For 2CXM the obtained value was the smallest one, smaller even from eGFR, whereas for ETK model it was almost the same as for eGFR.

Concerning the measurements dispersion, the broader limits of agreement for each of the PK models than those of eGFR indicate lower precision. 2CXM model was found the most precise one with LoA only broader by 5 mL/min/1.73 m<sup>2</sup>.

The accuracy and precision can be then combined in one metric, which is P30.

According to the National Kidney Foundation, the estimated GFR value within  $\pm 30\%$  of the true GFR value is sufficient for the clinical use. In the same time, it advises that at least 90% of the measurements obtained by the potential method should lay in this range to be considered as the accurate and precise enough ( $P30 \leq 90\%$ ) [67]. From the examined PK models, only 2CXM fulfils this condition with the  $P30 = 100\%$  comparable with the SCr blood test. The TK and ETK obtained 70% and 80% respectively.

Pearson correlations of eGFR, TK, ETK and 2CXM from mGFR were respectively  $r = 0.81$ ,  $r = -0.04$ ,  $r = -0.12$  and  $r = 0.51$ . Strong positive correlation was observed only for eGFR and 2CXM model, however, assuming the significance level of 5%, the linear dependency can be considered statistically significant only for eGFR. All p-values obtained for PK models much exceed 0.05.

Further, regarding the goodness of fit of the data, again 2CXM model showed the best results obtaining the smallest  $RMSE = 5.15 \text{ mL/min}/1.73 \text{ m}^2$ , which means that it provides the best description of renal parenchyma.

In conclusion, the 2CXM proved overall the best performance from the examined PK models in terms of both accuracy and precision, as well as the goodness of fit. Even though it obtained slightly worse precision than clinically used SCr test, it can be considered a method of GFR estimation, however, the tests on more data are recommended.

There can be several factors identified as a source of error influencing accuracy and precision of all models. In some DCE-MRI sequences the inflow artifact of the aorta was observed distorting the true AIF being the basis of the PK modelling. What is more, because of the lack of the  $T_{10}$  values and low doses of CA, the linear relationship between the signal intensity and CA concentration was assumed, which is only an approximation, not always perfectly true. More accurate measurements require conversion of signal intensity according to Formula (4.14). Next, some studies

suggest applying tracer kinetic theory separately to renal cortex and medulla [68, 69], however poor resolution of the MRI sequences disabled accurate segmentation of these compartments. In some cases it was even difficult to distinguish some regions of the kidney from the liver or adrenal gland organoleptically. Further, the hematocrit value used for calculation of the CA concentration in blood plasma was fixed as the average value for the healthy person. Tofts et al. [70] showed that 1% deviation of the hematocrit results in GFR error of 0.72%. Although all the participants were reported healthy, hematocrit values can still vary as much as from 38% to 54% depending on the sex, age and diet [71]. Eliminating any of these factors should yet improve the performance of any PK model. Last but not least, one should remember that physiological values such as blood pressure, temperature or GFR are continuously varying depending on the current diet or health and there are some day-to-day differences observed even between values obtained in two iohexol-GFR tests.

## 7.1 Future work

As it was mentioned before, the overall long-term aim of the project is to develop the fast and accurate, entirely data-driven method of GFR estimation. Due to the fact that the most-time consuming steps in the assessment of renal function are the registration of DCE-MRI sequences (one dataset takes approx. 6 h) and manual labelling of the kidneys, it is inevitable to eliminate them from the target method.

This goal was already achieved by implementing the *Convolutional Neural Network* (CNN) for kidneys segmentation from raw unprocessed DCE-MRI images and showed very promising results. More on this topic can be found in Appendix A. Further plans include automatic segmentation of the aorta and renal pelvis with CNN. If it turns out to be a success, in the last step the developed package for PK modelling will be applied in order to fit obtained time courses to 2CXM PK model.

# Chapter 8

## Summary

The main purposes of this thesis were, firstly, to design a library in the Python programming language for pharmacokinetic modelling from DCE-MRI images, which is to be incorporated into the fast method of GFR estimation, and secondly, to compare the performance of the few PK models for application of assessing renal function and to examine whether any of them can be considered accurate and precise enough to be used in the target method.

As a first step, the DCE-MRI sequences were registered in a time domain and both kidneys as well as aorta were manually labelled. Next, the renal pelvis was removed from the kidneys' labels on the basis of voxels' intensity time courses. For this purpose the PCA together with k-means clustering was applied. Subsequently, the average time-intensity curves were obtained for both kidneys and aorta. The signal intensity was converted into concentration by finding the temporal point, at which positive  $S'(t)$  reaches the maximum value. So obtained concentration time courses were then fitted to four pharmacokinetic models: Tofts Kermode, extended Tofts Kermode, Patlak-Rutland and two-compartment exchange models. Finally, on the basis of the obtained parameters the SKGFR as well as total GFR were calculated and compared with two chemical methods.

The developed algorithm was tested on the DCE-MRI sequences of ten different participants. Dice similarity coefficient of the pelvis segmentation was equal to  $DC = 0.86 \pm 0.06$ . For each of the sequence the pelvis was removed correctly without the need of manual correction. Regarding the performance of different PK models, the obtained results show that 2CXM is the most accurate and precise one and gives results comparable with those of the SCr blood test, which is a commonly used clinical method. What is more, the obtained  $P30 = 100\%$  for this model proves that its estimation is sufficient to be used in clinical use.

All in all, the thesis was a success. An important contribution is creating the module in Python, which will be used in further research on fast method of GFR estimation. On the basis of the drawn conclusions of practical tests the 2CXM model can be applied as a final step of the target method.

The source code is available at <https://github.com/KasiaSprawka>.

# Bibliography

- [1] G. Maio, "The metaphorical and mythical use of the kidney in antiquity," *American journal of nephrology*, vol. 19, no. 2, pp. 101–106, 1999.
- [2] K. Saladin, *Anatomy & Physiology: The Unity of Form and Function*. USA: McGraw-Hill, 5th ed., 2009.
- [3] V. Jha, G. Garcia-Garcia, K. Iseki, Z. Li, S. Naicker, B. Plattner, R. Saran, A. Y.-M. Wang, and C.-W. Yang, "Chronic kidney disease: global dimension and perspectives," *The Lancet*, vol. 382, no. 9888, pp. 260–272, 2013.
- [4] M. J. Sarnak, A. S. Levey, A. C. Schoolwerth, J. Coresh, B. Culleton, L. L. Hamm, P. A. McCullough, B. L. Kasiske, E. Kelepouris, M. J. Klag, *et al.*, "Kidney disease as a risk factor for development of cardiovascular disease," *Circulation*, vol. 108, no. 17, pp. 2154–2169, 2003.
- [5] National Kidney Foundation, "Kidney Disease: the basics." [Online]. Available: <https://www.kidney.org/news/newsroom/factsheets/KidneyDiseaseBasics>. [Accessed: 13-Nov-2017].
- [6] J. Traynor, R. Mactier, C. C. Geddes, and J. G. Fox, "How to measure renal function in clinical practice," *BMJ: British Medical Journal*, vol. 333, no. 7571, p. 733, 2006.
- [7] P. Delanaye, "How measuring glomerular filtration rate? comparison of reference methods," in *Basic Nephrology and Acute Kidney Injury*, InTech, 2012.
- [8] L. Bokacheva, H. Rusinek, J. L. Zhang, and V. S. Lee, "Assessment of renal function with dynamic contrast-enhanced MR imaging," *Magnetic resonance imaging clinics of North America*, vol. 16, no. 4, pp. 597–611, 2008.

- [9] F. Khalifa, A. Soliman, A. El-Baz, M. Abou El-Ghar, T. El-Diasty, G. Gimel'farb, R. Ouseph, and A. C. Dwyer, "Models and methods for analyzing DCE-MRI: A review," *Medical physics*, vol. 41, no. 12, 2014.
- [10] K. Patton and G. Thibodeau, *The Human Body in Health & Disease*. USA: Elsevier, 7th ed., 2017.
- [11] S. A. Emamian, M. B. Nielsen, J. F. Pedersen, and L. Ytte, "Kidney dimensions at sonography: correlation with age, sex, and habitus in 665 adult volunteers," *AJR. American journal of roentgenology*, vol. 160, no. 1, pp. 83–86, 1993.
- [12] Kidney Research UK, "Living with one kidney." [Online]. Available: <https://www.kidneyresearchuk.org/health-information/living-with-one-kidney>. [Accessed: 14-Feb-2018].
- [13] B. M. Koeppen and B. A. Stanton, *Renal Physiology: Mosby Physiology Monograph Series*. USA: Elsevier-Health Sciences Division, 5th ed., 2013.
- [14] P. Sturkie, "Kidneys, extrarenal salt excretion, and urine," in *Avian physiology*, pp. 359–382, Springer, 1986.
- [15] E. Jéquier and F. Constant, "Water as an essential nutrient: the physiological basis of hydration," *European journal of clinical nutrition*, vol. 64, no. 2, p. 115, 2010.
- [16] A. C. Guyton, T. G. Coleman, A. W. Cowley, K. W. Scheel, R. D. Manning, and R. A. Norman, "Arterial pressure regulation: overriding dominance of the kidneys in long-term regulation and in hypertension," *The American journal of medicine*, vol. 52, no. 5, pp. 584–594, 1972.
- [17] L. L. Hamm, N. Nakhoul, and K. S. Hering-Smith, "Acid-base homeostasis," *Clinical Journal of the American Society of Nephrology*, vol. 10, no. 12, pp. 2232–2242, 2015.
- [18] S. Donnelly, "Why is erythropoietin made in the kidney? the kidney functions as a critmeter," *American journal of kidney diseases*, vol. 38, no. 2, pp. 415–425, 2001.

- [19] S. Williams, K. Malatesta, and K. Norris, "Vitamin D and chronic kidney disease," *Ethnicity & disease*, vol. 19, no. 4 Suppl 5, p. S5, 2009.
- [20] E. Newsholme and W. Gevers, "Control of glycolysis and gluconeogenesis in liver and kidney cortex," in *Vitamins & Hormones*, vol. 25, pp. 1–87, Elsevier, 1967.
- [21] The Free Dictionary: medical dictionary, "Glomerular filtration rate." [Online]. Available: <https://medical-dictionary.thefreedictionary.com/glomerular+filtration+rate>. [Accessed: 01-Feb-2017].
- [22] H. W. Smith, *The Kidney: Structure and Function in Health and Disease*, vol. 1. Oxford University Press, USA, 1951.
- [23] J. R. Weinstein and S. Anderson, "The aging kidney: physiological changes," *Advances in chronic kidney disease*, vol. 17, no. 4, pp. 302–307, 2010.
- [24] National Kidney Foundation, "Glomerular Filtration Rate (GFR)." [Online]. Available: <https://www.kidney.org/atoz/content/gfr>. [Accessed: 13- Nov-2017].
- [25] Khanacademy, "Renal physiology: Glomerular filtration." [Online]. Available: <https://www.khanacademy.org/test-prep/mcat/organ-systems/the-renal-system/a/renal-physiology-glomerular-filtration>. [Accessed: 12-Feb-2017].
- [26] W. C. Röntgen, "On a new kind of rays," *Science*, vol. 3, no. 59, pp. 227–231, 1896.
- [27] J. D. Bronzino, *The Biomedical Engineering Handbook*, vol. 2. CRC press, 1999.
- [28] S. Conolly et al., *The Biomedical Engineering Handbook*, ch. Magnetic Resonance Imaging. Vol. 2 of [27], 1999.
- [29] V. P. Grover, J. M. Tognarelli, M. M. Crossey, I. J. Cox, S. D. Taylor-Robinson, and M. J. McPhail, "Magnetic resonance imaging: principles and techniques: lessons for clinicians," *Journal of clinical and experimental hepatology*, vol. 5, no. 3, pp. 246–255, 2015.

- [30] S. C. Bushong and G. Clarke, *Magnetic resonance imaging: physical and biological principles*. Elsevier Health Sciences, 2014.
- [31] Startradiology, “MRI Technique.” [Online]. Available: <http://www.startradiology.com/the-basics/mri-technique/>. [Accessed: 12-Feb-2017].
- [32] R. Sharma, S. Fulzele, K. Shetty, M. Sachdeva, and B. R. Locke, “21 Tesla Micro-MRI of Rat Skin,” 2008.
- [33] S. Hidalgo-Tobon, “Theory of gradient coil design methods for magnetic resonance imaging,” *Concepts in Magnetic Resonance Part A*, vol. 36, no. 4, pp. 223–242, 2010.
- [34] St. Vincent’s University Hospital. Radiology Departament, “MRI.” [Online]. Available: <http://www.svuhradiology.ie/diagnostic-imaging/mri/>. [Accessed: 12-Feb-2017].
- [35] WebMD, “What Is an MRI?.” [Online]. Available: <https://www.webmd.com/a-to-z-guides/what-is-an-mri#1>. [Accessed: 08-Feb-2018].
- [36] A. Jackson, D. L. Buckley, G. J. Parker, *et al.*, *Dynamic contrast-enhanced magnetic resonance imaging in oncology*. Springer, 2005.
- [37] S. L. Barnes, J. G. Whisenant, M. E. Loveless, and T. E. Yankeelov, “Practical dynamic contrast enhanced MRI in small animal models of cancer: data acquisition, data analysis, and interpretation,” *Pharmaceutics*, vol. 4, no. 3, pp. 442–478, 2012.
- [38] L. E. Gerlowski and R. K. Jain, “Physiologically based pharmacokinetic modeling: principles and applications,” *Journal of pharmaceutical sciences*, vol. 72, no. 10, pp. 1103–1127, 1983.
- [39] L. K. Paalzow, “Torsten teorell, the father of pharmacokinetics,” *Upsala journal of medical sciences*, vol. 100, no. 1, pp. 41–46, 1995.
- [40] S. Sourbron, “Compartmental modelling for magnetic resonance renography,” *Zeitschrift fur medizinische Physik*, vol. 20, no. 2, p. 101—114, 2010.
- [41] S. Riedel, “Pharmacokinetic Modelling for Dynamic Contrast-Enhanced MR Renography,” Bachelor’s thesis, University of Lübeck, December 2012.

- [42] S. P. Sourbron and D. L. Buckley, "On the scope and interpretation of the Tofts models for DCE-MRI," *Magnetic resonance in medicine*, vol. 66, no. 3, pp. 735–745, 2011.
- [43] P. S. Tofts and A. G. Kermode, "Measurement of the blood-brain barrier permeability and leakage space using dynamic mr imaging. 1. fundamental concepts," *Magnetic resonance in medicine*, vol. 17, no. 2, pp. 357–367, 1991.
- [44] P. S. Tofts, "Modeling tracer kinetics in dynamic Gd-DTPA MR imaging," *Journal of magnetic resonance imaging*, vol. 7, no. 1, pp. 91–101, 1997.
- [45] C. S. Patlak, R. G. Blasberg, and J. D. Fenstermacher, "Graphical evaluation of blood-to-brain transfer constants from multiple-time uptake data," *Journal of Cerebral Blood Flow & Metabolism*, vol. 3, no. 1, pp. 1–7, 1983.
- [46] Simens Healthineers, "Magnetom avanto." [Online]. Available: <https://www.healthcare.siemens.com/magnetic-resonance-imaging/0-35-to-1-5t-mri-scanner/magnetom-avanto> [Accessed: 13- Nov- 2017].
- [47] E. Eikefjord, E. Andersen, E. Hodneland, E. A. Hanson, S. Sourbron, E. Svarstad, A. Lundervold, and J. T. Rørvik, "Dynamic contrast-enhanced MRI measurement of renal function in healthy participants," *Acta Radiologica*, vol. 58, no. 6, pp. 748–757, 2017.
- [48] X. Yang, H. Le Minh, K.-T. T. Cheng, K. H. Sung, and W. Liu, "Renal compartment segmentation in DCE-MRI images," *Medical image analysis*, vol. 32, pp. 269–280, 2016.
- [49] R Development Core Team, *R: A Language and Environment for Statistical Computing*. R Foundation for Statistical Computing, Vienna, Austria, 2008. ISBN 3-900051-07-0.
- [50] B. B. Avants, B. M. Kandel, J. T. Duda, P. A. Cook, N. J. Tustison, and S. KL, *ANTsR: ANTs in R: quantification tools for biomedical images*, 2016. R package version 0.3.3.
- [51] B. B. Avants, N. J. Tustison, G. Song, P. A. Cook, A. Klein, and J. C. Gee, "A reproducible evaluation of ANTs similarity metric performance in brain image registration," *Neuroimage*, vol. 54, no. 3, pp. 2033–2044, 2011.

- [52] B. B. Avants, C. L. Epstein, M. Grossman, and J. C. Gee, "Symmetric diffeomorphic image registration with cross-correlation: evaluating automated labeling of elderly and neurodegenerative brain," *Medical image analysis*, vol. 12, no. 1, pp. 26–41, 2008.
- [53] F. E.-Z. A. El-Gamal, M. Elmogy, and A. Atwan, "Current trends in medical image registration and fusion," *Egyptian Informatics Journal*, vol. 17, no. 1, pp. 99–124, 2016.
- [54] P. A. Yushkevich, J. Piven, H. Cody Hazlett, R. Gimpel Smith, S. Ho, J. C. Gee, and G. Gerig, "User-Guided 3D Active Contour Segmentation of Anatomical Structures: Significantly Improved Efficiency and Reliability," *Neuroimage*, vol. 31, no. 3, pp. 1116–1128, 2006.
- [55] Python Core Team, *Python: A dynamic, open source programming language*. Python Software Foundation, 2015.
- [56] J. E. Jackson, *A user's guide to principal components*, vol. 587. John Wiley & Sons, 2005.
- [57] G. H. Duntzman, *Principal components analysis*. No. 69, Sage, 1989.
- [58] I. T. Jolliffe, "Principal component analysis and factor analysis," in *Principal component analysis*, pp. 115–128, Springer, 1986.
- [59] A. Géron, *Hands-On Machine Learning with Scikit-Learn and TensorFlow*. USA: O'Reilly Media, 2017.
- [60] J. MacQueen *et al.*, "Some methods for classification and analysis of multivariate observations," in *Proceedings of the fifth Berkeley symposium on mathematical statistics and probability*, vol. 1, pp. 281–297, Oakland, CA, USA., 1967.
- [61] K. Alsabti, S. Ranka, and V. Singh, "An efficient k-means clustering algorithm," 1997.
- [62] M. Ryan, *Calculus Workbook For Dummies*. USA: Wiley Publishing, 2nd ed., 2005.
- [63] P. S. Tofts, "T1-weighted DCE imaging concepts: modelling, acquisition and analysis," *signal*, vol. 500, no. 450, p. 400, 2010.

- [64] P. S. Tofts, G. Brix, D. L. Buckley, J. L. Evelhoch, E. Henderson, M. V. Knopp, H. B. Larsson, T.-Y. Lee, N. A. Mayr, G. J. Parker, *et al.*, "Estimating kinetic parameters from dynamic contrast-enhanced T1-weighted MRI of a diffusible tracer: standardized quantities and symbols," *Journal of magnetic resonance imaging*, vol. 10, no. 3, pp. 223–232, 1999.
- [65] L. R. Dice, "Measures of the amount of ecologic association between species," *Ecology*, vol. 26, no. 3, pp. 297–302, 1945.
- [66] J. M. Bland and D. Altman, "Statistical methods for assessing agreement between two methods of clinical measurement," *The lancet*, vol. 327, no. 8476, pp. 307–310, 1986.
- [67] A. S. Levey, J. Coresh, E. Balk, A. T. Kausz, A. Levin, M. W. Steffes, R. J. Hogg, R. D. Perrone, J. Lau, and G. Eknayan, "National kidney foundation practice guidelines for chronic kidney disease: evaluation, classification, and stratification," *Annals of internal medicine*, vol. 139, no. 2, pp. 137–147, 2003.
- [68] D. Baumann and M. Rudin, "Quantitative assessment of rat kidney function by measuring the clearance of the contrast agent Gd (DOTA) using dynamic MRI," *Magnetic resonance imaging*, vol. 18, no. 5, pp. 587–595, 2000.
- [69] V. S. Lee, H. Rusinek, L. Bokacheva, A. J. Huang, N. Oesingmann, Q. Chen, M. Kaur, K. Prince, T. Song, E. L. Kramer, *et al.*, "Renal function measurements from MR renography and a simplified multicompartmental model," *American Journal of Physiology-Renal Physiology*, vol. 292, no. 5, pp. F1548–F1559, 2007.
- [70] P. S. Tofts, M. Cutajar, I. A. Mendichovszky, A. M. Peters, and I. Gordon, "Precise measurement of renal filtration and vascular parameters using a two-compartment model for dynamic contrast-enhanced mri of the kidney gives realistic normal values," *European radiology*, vol. 22, no. 6, pp. 1320–1330, 2012.
- [71] W. SHIEL, "Hematocrit." [Online]. Available: [https://www.medicinenet.com/hematocrit/article.htm#what\\_is\\_the\\_hematocrit](https://www.medicinenet.com/hematocrit/article.htm#what_is_the_hematocrit). [Accessed: 02-Apr-2018].
- [72] "ECR 2018 - book of abstracts," *Insights into Imaging*, Feb 2018.

# Appendix A

Below attached the abstract accepted for *European Congress of Radiology 2018* [72]:

**B-0484** 11:34

**Fast estimation of kidney volumes and time courses in DCE-MRI using convolutional neural networks**

A.S. Lundervold<sup>1</sup>, K. Sprawka<sup>2</sup>, A. Lundervold<sup>1</sup>; <sup>1</sup>*Bergen/NO*, <sup>2</sup>*Lodz/PL*  
(allu@hvl.no)

**Purpose:** We create a novel method for fast and accurate estimation of kidney volumes and signal intensity time courses in DCE-MRI, aiming at extracting both structural and functional quantitative information from the moving kidney.

**Methods and Materials:** Two repeated SPGR-DCE-MRI datasets were acquired from 20 healthy volunteers, resulting in 40 examinations, each consisting of 74 volumes recorded over ~6 min. We trained a 3D convolutional neural network (using a single standard NVIDIA GeForce 1080Ti GPU) for segmentation of left and right kidneys. The network has a dual-pathway architecture, incorporating both local and global information in the volumes. To create training data, we manually delineated 10 individual volumes from 10 different time-series, and extended the delineations to 740 volumes using image registration.

**Results:** Our implementation is able to segment all 74 volumes in a previously unseen, unregistered recording in less than 7 minutes. Mean segmentation accuracy (Dice) was 0.843 (SD=0.010). Mean (SD) left and right kidney volumes [ml] (incl. renal hilum) in one of the subjects (FF03) examined seven days apart (MR1 and MR2) was: MR1 L: 301.6 (15.9), R: 389.8 (16.9); MR2 L: 307.4 (17.8) R: 395.3 (23.6).

**Conclusion:** A CNN is able to quickly and accurately segment the moving kidneys in DCE-MRI, providing estimates of kidney volumes and mean signal intensity time courses. We are currently working to achieve sub-segmentation of the kidney (cortex, medulla, pelvis) and segmentation of the aorta (for AIF), enabling automated and fast estimation of GFR directly from the DCE-MRI.

# Appendix B

The CD attached to this thesis contains:

- Electronic version of the thesis
- Microsoft Excel file with the test results
- NIfTI files of the sample subject: original DCE-MRI sequence, motion corrected sequence, file with the labels of both kidneys and aorta, file with the labels of both kidney with removed pelvis and aorta

# List of Figures

2.1	Gross kidney anatomy . . . . .	6
2.2	The structure of the nephron . . . . .	8
2.3	Process of the urine formation . . . . .	11
2.4	GFR reference values . . . . .	12
3.1	Hydrogen atoms placed in the magnetic field . . . . .	15
3.2	Precessional motion of the atom in the magnetic field . . . . .	16
3.3	$T_1$ and $T_2$ contrast mechanisms . . . . .	18
3.4	Comparison of $T_1$ - and $T_2$ -weighted images . . . . .	19
3.5	DCE-MRI enhancement patterns . . . . .	21
3.6	Sample parameters used in semi-quantitative DCE-MRI analysis . .	22
4.1	Teorell's first PK model . . . . .	26
4.2	An arbitrary multi-compartment model . . . . .	27
5.1	Sample DCE-MRI sequence of the healthy kidneys. . . . .	36
5.2	Sample labels of kidneys and aorta . . . . .	39
5.3	Example kidney compartments time courses . . . . .	40
5.4	Principal component analysis for a sample kidney . . . . .	41
5.5	Average time courses for two clusters detected in k-means algorithm	43
5.6	Sample kidney segmentation with k-means clustering . . . . .	43
5.7	Sample average time-intensity curves for a kidney and aorta with marked last points of the baseline . . . . .	44

5.8	Sample average time-intensity curves for a kidney and aorta with applied median filter . . . . .	46
5.9	Positive derivative of the sample kidney and aorta intensity time courses	46
5.10	Time courses of a sample kidney and aorta after intensity-concentration conversion . . . . .	47
5.11	An example of models fit . . . . .	52
6.1	Bland–Altman plots for different methods . . . . .	57
6.2	Relation between mGFR and different estimation method . . . . .	59

# List of Tables

5.1	Clinical characteristics of the participants . . . . .	37
6.1	GFR values derived from DCE-MRI using different PK models and values obtained with chemical methods . . . . .	56
6.2	Comparison of different GFR estimation methods . . . . .	58